

# A new probe of magnetic fields in the pre-reionization epoch: II. Detectability

Vera Gluscevic,<sup>1</sup> Tejaswi Venumadhav,<sup>1</sup> Abhilash Mishra,<sup>2</sup> Antonija Oklopčić,<sup>2</sup> Xiao Fang,<sup>3</sup> and Christopher Hirata<sup>3</sup>

<sup>1</sup>*Institute for Advanced Study, Einstein Drive, Princeton, NJ 08540, USA*

<sup>2</sup>*California Institute of Technology, Mail Code 350-17, Pasadena, CA 91125, USA*

<sup>3</sup>*Center for Cosmology and Astroparticle Physics, The Ohio State University,*

*191 West Woodruff Lane, Columbus, Ohio 43210, USA*

(Dated: April 3, 2016)

In the first paper of this series, we proposed a novel method to probe large-scale intergalactic magnetic fields during the cosmic Dark Ages, using 21-cm tomography. In this paper, we examine sensitivity of future tomographic surveys to detecting magnetic fields using this method. We develop a minimum-variance estimator formalism to search for the characteristic anisotropic imprint of a magnetic field on the statistics of the 21-cm brightness-temperature fluctuations. We find that an array of dipole antennas in a compact-grid configuration, with a square kilometer of collecting area, would be sensitive to fields of strength  $\sim 10^{-21}$  Gauss comoving (scaled to present-day value), and reach almost ten orders of magnitude below the current constraints on primordial magnetic fields from the cosmic-microwave-background observations.

## I. INTRODUCTION

Magnetic fields are ubiquitous in the universe on all observed scales [1–5]. However, the origins of the magnetic fields in galaxies and on large scales are as of yet an unresolved question. Various forms of dynamo mechanism have been proposed to maintain and amplify magnetic fields [6], but they typically require the presence of seed fields [1]. Such seed fields may be produced during structure formation through the Biermann battery process or similar mechanisms [7, 8], or may otherwise be relics from the early universe [1, 9, 10]. Observations of large-scale low-strength magnetic fields in the high-redshift intergalactic medium (IGM) could thus probe the origins of present-day magnetic fields and potentially open up an entirely new window into the physics of the early universe.

Many observational probes have been previously proposed and used to search for evidence of large-scale magnetic fields locally and at high redshifts (e. g. [4, 11–19]). Amongst the most sensitive tracers of cosmological magnetic fields is the cumulative effect of Faraday rotation in the cosmic-microwave-background (CMB) polarization maps, which currently places an upper limit of  $\sim 10^{-10}$  Gauss (in comoving units) using data from the Planck satellite [20]. In Paper I of this series [21], we proposed a novel method to detect and measure extremely weak cosmological magnetic fields during the pre-reionization epoch (the cosmological Dark Ages). This method relies on data from upcoming and future 21-cm tomography surveys [22, 23], many of which have pathfinder experiments currently running [24–29], with the next-stage experiments planned for the coming decade [27, 29].

In Paper I, we calculated the effect of a magnetic fields on the statistics of the 21-cm signal, and in this paper (which we refer to as Paper II in the following), we focus on evaluating the sensitivity of future 21-cm experiments to this effect. As we discussed in Paper I, measurement of statistical anisotropy in the 21-cm signal from the Dark Ages has an intrinsic sensitivity to magnetic fields in the

IGM more than *ten orders of magnitude below the current upper limits from the CMB*. In the following, we demonstrate that a square-kilometer array of dipole antennas in a compact grid can reach the sensitivity necessary to detect large-scale magnetic fields that are on the order of  $10^{-21}$  Gauss comoving (scaled to present day, assuming adiabatic evolution of the field due to Hubble expansion).

The rest of this paper is organized as follows. In §II, we summarize the main results of Paper I. In §III, we define our notation and review the basics of the 21-cm signal and its measurement. In §IV, we derive minimum-variance estimators for uniform and stochastic magnetic fields. In §V, we set up the Fisher analysis formalism necessary to evaluate detectability. In §VI, we present numerical results, and we conclude in §VII. Supporting materials are presented in the appendices.

## II. SUMMARY OF THE METHOD

Magnetic moments of hydrogen atoms in the triplet state of the 21-cm line transition tend to align with the incident quadrupole of the 21-cm radiation from the surrounding medium. This effect of “ground-state alignment” [30, 31] arises in a cosmological setting due to velocity-field gradients. In the presence of an external magnetic field, the emitted 21-cm quadrupole is misaligned with the incident quadrupole, due to atomic precession (illustrated in Figure 1). The resulting emission anisotropy can thus be used to trace magnetic fields at high redshifts.

The main result of Paper I was a calculation of the 21-cm brightness-temperature  $T$  fluctuation<sup>1</sup> as a function of the line-of-sight direction  $\hat{n}$ , in the frame of the

---

<sup>1</sup> Standard notation, used in other literature and in Paper I of this series, for this quantity is  $\delta T_b$ ; however, we use  $T$  here to simplify our expressions.



Figure 1. Illustration of the effect of a magnetic field on hydrogen atoms in the excited state of 21-cm transition at high redshifts. In the classical picture, magnetic moments of the atoms (depicted as red arrows) tend to be aligned with density gradients (upper panel; the gradient is depicted with the background shading), unless they precess about the direction of ambient magnetic field (pointing out of the page on the lower panel). When the precessing atoms decay back into the ground state, the emitted quadrupole (aligned with the direction of the magnetic moments) is misaligned with the incident quadrupole. This offset can be observed as a statistical anisotropy in 21-cm brightness-temperature signal, and used to trace cosmological magnetic fields.

emitting ensemble of atoms. The key result there is

$$\begin{aligned}
 T(\hat{\mathbf{n}}, \hat{\mathbf{k}}) = & \left(1 - \frac{T_\gamma}{T_s}\right) x_{1s} \left(\frac{1+z}{10}\right)^{1/2} \\
 & \times \left[ 26.4 \text{ mK} \left\{ 1 + \left( \hat{\mathbf{k}} \cdot \hat{\mathbf{n}} \right)^2 \right\} \delta \right] - 0.128 \text{ mK} \left( \frac{T_\gamma}{T_s} \right) \\
 & \times x_{1s} \left( \frac{1+z}{10} \right)^{1/2} \left\{ 1 + 2 \left( 1 + \left( \hat{\mathbf{k}} \cdot \hat{\mathbf{n}} \right)^2 \right) \delta \right. \\
 & \left. - \frac{\delta}{15} \sum_m \frac{4\pi}{5} \frac{Y_{2m}(\hat{\mathbf{k}}) [Y_{2m}(\hat{\mathbf{n}})]^*}{1 + x_{\alpha,(2)} + x_{c,(2)} - imx_B} \right\}, \quad (1)
 \end{aligned}$$

where the magnetic field is along the  $z$  axis;  $x_{\alpha,(2)}$ ,  $x_{c,(2)}$  and  $x_B$  parametrize the rates of depolarization of the ground state by optical pumping and atomic collisions, and the rate of magnetic precession (relative to radiative depolarization), respectively (defined in detail in Paper I). Furthermore,  $T_s$  and  $T_\gamma$  are the spin temperature

and the CMB temperature at redshift  $z$ , respectively;  $\hat{\mathbf{k}}$  is a unit vector in the direction of the wave-vector  $\vec{k}$  of a given density Fourier mode; and  $Y_{2m}$  represent the usual spin-zero spherical harmonics. Figure 2 illustrates the effect of the magnetic field on the brightness temperature emission pattern in the frame of the atom; shown are quadrupole patterns corresponding to the last term of Eq. (1), for various strengths of the magnetic field. Notice that there is a saturation limit for the field strength—for a strong field, the precession is much faster than the decay of the excited state, and the emission pattern asymptotes to the one shown in the bottom panel of Figure 2. Above this limit, as discussed in later Sections, the signal cannot be used to reconstruct the strength of the field; however, in the saturated regime, it is still possible to distinguish presence of a strong magnetic field from the case of no magnetic field, as we discuss in detail in §V.

The effect of quadrupole misalignment arises at second order in optical depth (it is a result of a two-scattering process), and is thus a small correction to the total brightness temperature. However, owing to the long lifetime of the excited state (during which even an extremely slow precession has a large cumulative effect on the direction of the quadrupole at second order), the misalignment is exquisitely sensitive to magnetic fields in the IGM at redshifts prior to cosmic reionization. As we showed in Paper I, a minuscule magnetic field of  $10^{-21}$  Gauss (in comoving units) produces order-one changes in the direction of the quadrupole. This implies that a high-precision measurement of the 21-cm brightness-temperature 2-point correlation function intrinsically has that level of sensitivity to magnetic fields in the Dark Ages. We now proceed to develop a formalism to search for this effect with surveys of redshifted 21-cm line, and to identifying experimental setups that can achieve this goal.

### III. BASICS

Before focusing on the estimator formalism in the next Section, here we review the basics of 21-cm brightness temperature fluctuation measurements. In §III A, we setup our notation and review definitions of quantities describing sensitivity of interferometric radio arrays; in §III B, we focus on the derivation of the noise power spectrum; and in §III C, we discuss the effects of the array configuration and its relation to coverage of modes in the  $uv$  plane.

#### A. Definitions

The redshifted 21-cm signal can be represented with specific intensity at a location in physical space  $I(\vec{r})$  or in Fourier space  $\tilde{I}(\vec{k})$ . In sky coordinates (centered on an emitting patch of the sky), these functions become

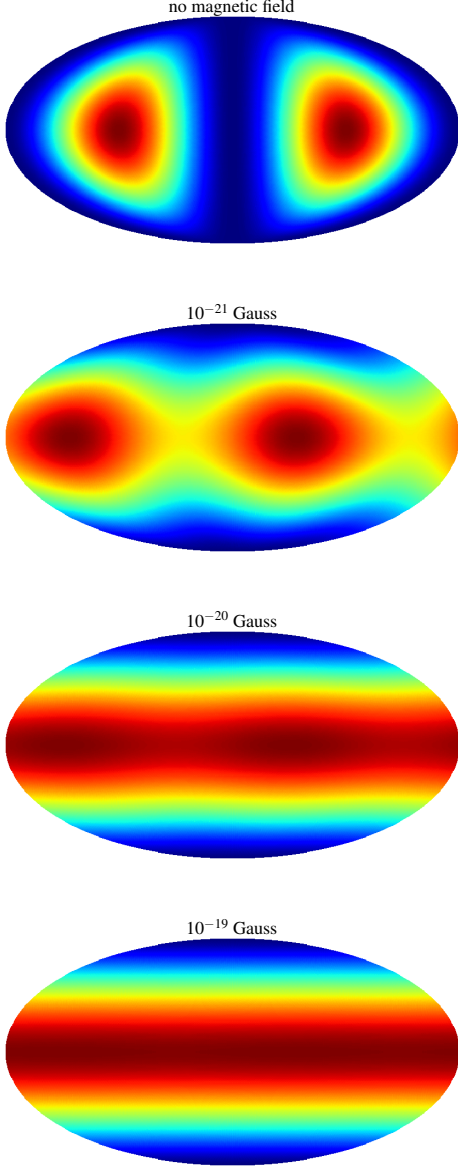


Figure 2. Illustration of the quadrupolar pattern of 21-cm emission from the last ( $\vec{B}$ -dependent) term of Eq. (1) in the frame of the emitting atoms, for the case where  $\vec{k}$  is perpendicular to  $\hat{\mathbf{n}}$  (maximal signal), shown in Molleweide projection. Lower panels correspond to increasingly stronger magnetic fields (strength denoted on each panel in comoving units), with the bottom panel corresponding to the saturated case. Notice how the type of quadrupole in the top panel (“weak-field” regime) is distinct from that in the bottom panel (“strong-field” regime).

$\mathcal{I}(\theta_x, \theta_y, \theta_\nu)$  and  $\tilde{\mathcal{I}}(u, v, \eta)$ , respectively. Here, vector  $\vec{k}$  (in the units of comoving  $\text{Mpc}^{-1}$ ) is a Fourier dual of  $\vec{r}$  (comoving Mpc), and likewise,  $\theta_x$  (rad),  $\theta_y$  (rad), and  $\theta_\nu$  (Hz) are duals of the coordinates  $u$  ( $\text{rad}^{-1}$ ),  $v$  ( $\text{rad}^{-1}$ ), and  $\eta$  (seconds), respectively. Notice that  $\theta_x$  and  $\theta_y$  represent the angular extent of the patch in the sky, while

$\theta_\nu$  represents its extent in frequency space. The two sets of coordinates are related through linear transformations in the following way

$$\begin{aligned}\theta_x &= \frac{r_x}{\chi(z)}, & u &= \frac{k_x \chi(z)}{2\pi}, \\ \theta_y &= \frac{r_y}{\chi(z)}, & v &= \frac{k_y \chi(z)}{2\pi}, \\ \theta_\nu &= \frac{H(z) \nu_{21}}{c(1+z)^2} r_z, & \eta &= \frac{c(1+z)^2}{2\pi H(z) \nu_{21}} k_z,\end{aligned}\quad (2)$$

where  $\nu_{21}$  is the 21-cm frequency in the rest frame of emitting atoms,  $H(z)$  is the Hubble parameter,  $\chi(z)$  is the comoving distance to redshift  $z$ , which marks the middle of the observed data cube (where  $r_z$  and  $\theta_\nu$  intervals are evaluated). Note that  $2\pi\theta_i u = r_i k_i$ , for  $i \in \{x, y\}$ . The convention we use for the Fourier transforms is

$$\begin{aligned}I(\vec{r}) &= \frac{1}{(2\pi)^3} \int \tilde{I}(\vec{k}) e^{i\vec{k} \cdot \vec{r}} d\vec{k}, \\ \tilde{I}(\vec{k}) &= \int I(\vec{r}) e^{-i\vec{k} \cdot \vec{r}} d\vec{r},\end{aligned}\quad (3)$$

where Fourier-space functions are denoted with tilde. Similarly,

$$\begin{aligned}\mathcal{I}(\theta_x, \theta_y, \theta_\nu) &= \int \tilde{\mathcal{I}}(u, v, \eta) e^{2\pi i(u\theta_x + v\theta_y + \eta\theta_\nu)} du dv d\eta, \\ \tilde{\mathcal{I}}(u, v, \eta) &= \int \mathcal{I}(\theta_x, \theta_y, \theta_\nu) e^{-2\pi i(u\theta_x + v\theta_y + \eta\theta_\nu)} d\theta_x d\theta_y d\theta_\nu.\end{aligned}\quad (4)$$

From Eqs. (2)–(4), we can see that the following scaling relation is satisfied

$$\tilde{I}(\vec{k}) = \frac{c(1+z)^2 \chi(z)^2}{H(z) \nu_{21}} \tilde{\mathcal{I}}(u, v, \eta), \quad (5)$$

where the proportionality factor contains the transformation Jacobian  $\frac{dr_x dr_y dr_z}{d\theta_x d\theta_y d\theta_\nu}$ . Finally, the relationship between the specific intensity in the  $uv$ -plane and the visibility function  $V(u, v, \theta_\nu)$  is given by the Fourier transform of the frequency coordinate,

$$\begin{aligned}\mathcal{V}(u, v, \theta_\nu) &= \int \tilde{\mathcal{I}}(u, v, \eta) e^{2\pi i \theta_\nu \eta} d\eta, \\ \tilde{\mathcal{I}}(u, v, \eta) &= \int \mathcal{V}(u, v, \theta_\nu) e^{-2\pi i \theta_\nu \eta} d\theta_\nu.\end{aligned}\quad (6)$$

Here,  $\theta_{\nu, \text{max}} - \theta_{\nu, \text{min}} = \Delta\nu$  is the bandwidth of the observed data cube centered on  $z$  (see also Appendix A).

## B. Power spectra and noise

In this Section, we derive the noise power spectrum for the brightness temperature signal. We start by defining a brightness-temperature power spectrum as

$$\langle \tilde{I}(\vec{k}) \tilde{I}^*(\vec{k}') \rangle \equiv (2\pi)^3 P_{\tilde{I}} \delta_D(\vec{k} - \vec{k}'), \quad (7)$$

where  $\delta_D$  is Dirac delta function. The observable quantity of the interferometric arrays is the visibility function—a complex Gaussian variable with a zero mean and the following variance (derived in Appendix A)

$$\begin{aligned} & \langle \mathcal{V}(u, v, \theta_\nu) \mathcal{V}(u', v', \theta'_\nu)^* \rangle \\ &= \frac{1}{\Omega_{\text{beam}}} \left( \frac{2k_B T_{\text{sky}}}{A_e \sqrt{\Delta\nu t_1}} \right)^2 \delta_D(u - u') \delta_D(v - v') \delta_{\theta_\nu, \theta'_\nu}, \end{aligned} \quad (8)$$

where  $T_{\text{sky}}$  is the sky temperature (that in principle includes both the foreground signal from the Galaxy, and the instrument noise, where we take the latter to be subdominant in §VI);  $t_1$  is the total time a single baseline observes element  $(u, v)$  in the  $uv$  plane;  $A_e$  is the collecting area of a single dish;  $k_B$  is the Boltzmann constant;  $\Delta\nu$  is the bandwidth of a single observation centered on  $z$ ; and the last  $\delta$  in this expression denotes the Kronecker delta.

In the next step, we to combine Eqs. (6) and (8), and take the ensemble average,

$$\begin{aligned} & \langle \tilde{\mathcal{I}}(u, v, \eta) \tilde{\mathcal{I}}^*(u', v', \eta') \rangle \\ &= \frac{1}{t_1 \Omega_{\text{beam}}} \left( \frac{2k_B T_{\text{sky}}}{A_e} \right)^2 \delta_D(u - u') \delta_D(v - v') \delta_D(\eta - \eta'), \end{aligned} \quad (9)$$

where we used

$$\int e^{2\pi i \theta_\nu (\eta - \eta')} d\theta_\nu = \delta_D(\eta - \eta'). \quad (10)$$

Taking into account the scaling relation of Eq. (5), using Eq. (7), and keeping in mind the scaling property of the delta function, we arrive at

$$P_1^N(\vec{k}) = \frac{c(1+z)^2 \chi^2(z)}{\Omega_{\text{beam}} t_1 H(z) \nu_{21}} \left( \frac{2k_B T_{\text{sky}}}{A_e} \right)^2, \quad (11)$$

for the noise power per  $\vec{k}$  mode, per baseline.

In the last step, we wish to get from Eq. (11) to the expression for the noise power spectrum that corresponds to observation with all available baselines. To do that, we need to incorporate information about the array configuration and its coverage of the  $uv$  plane. In other words, we need to divide the expression in Eq. (11) by the number density of baselines  $n_{\text{base}}(\vec{k})$  that observe a given mode  $\vec{k}$  at a given time (for a discussion of the  $uv$  coverage, see the following Section). The final result for the noise power spectrum per mode  $\vec{k}$  in the intensity units is

$$P^N(\vec{k}) = \frac{c(1+z)^2 \chi^2(z)}{\Omega_{\text{beam}} t_1 H(z) \nu_{21}} \frac{(2k_B T_{\text{sky}})^2}{A_e^2 n_{\text{base}}(\vec{k})}, \quad (12)$$

and in temperature units

$$P^N(\vec{k}) = \frac{\lambda^4 c(1+z)^2 \chi^2(z)}{\Omega_{\text{beam}} t_1 H(z) \nu_{21}} \frac{T_{\text{sky}}^2}{A_e^2 n_{\text{base}}(\vec{k})}, \quad (13)$$

where  $\lambda = c/\nu_{21}(1+z)$ .

### C. The UV coverage

Total number density  $n_{\text{base}}(\vec{k})$  of baselines that can observe mode  $\vec{k}$  is related to the (unitless) number density  $n(u, v)$  of baselines per  $dudv$  element as

$$n_{\text{base}}(\vec{k}) = \frac{n(u, v)}{\Omega_{\text{beam}}}, \quad (14)$$

where  $\frac{1}{\Omega_{\text{beam}}}$  represents an element in the  $uv$  plane. The number density integrates to the total number of baselines  $N_{\text{base}}$ ,

$$N_{\text{base}} = \frac{1}{2} N_{\text{ant}} (N_{\text{ant}} + 1) = \int_{\text{half}} n(u, v) dudv, \quad (15)$$

where  $N_{\text{ant}}$  is the number of antennas in the array, and the integration is done on the half of the  $uv$  plane (because the visibility has the following property  $V(u, v, \theta_\nu) = V^*(-u, -v, \theta_\nu)$ , and only half the plane contains independent samples). We assume that the array consists of many antennas, so that time-dependence of  $n(u, v)$  is negligible; if this is not the case, time average of this quantity should be computed to account for Earth's rotation.

In this work, we focus on a specific array configuration that is of particular interest to cosmology—a compact grid of dipole antennas, with a total collecting area  $(\Delta L)^2$ . This has been proposed for the Fast Fourier Transform Telescope (FFTT) [32] and is being implemented for Hydrogen Epoch of Reionization Array (HERA) [29], for example. In this case, the beam solid angle is 1 sr, the effective area of a single dipole is  $A_e = \lambda^2$ , and the effective number of antennas is  $N_{\text{ant}} = \frac{(\Delta L)^2}{\lambda^2}$ . For such configuration, the number density of baselines entering calculation of the noise power spectrum reads

$$n(u, v) = \left( \frac{\Delta L}{\lambda} - u \right) \left( \frac{\Delta L}{\lambda} - v \right). \quad (16)$$

The relation between  $\vec{k} = (k, \theta_k, \phi_k)$  and  $(u, v)$  is

$$\begin{aligned} u_\perp &\equiv \frac{\chi(z)}{2\pi} k \sin \theta_k, \\ u &= u_\perp \cos \phi_k, \\ v &= u_\perp \sin \phi_k, \end{aligned} \quad (17)$$

where subscript  $\perp$  denotes components perpendicular to the line-of-sight direction  $\hat{\mathbf{n}}$ , which, in this case, is along the  $z$  axis. From this, the corresponding number of baselines observing a given  $\vec{k}$  is

$$\begin{aligned} n_{\text{base}}(\vec{k}) &= \left( \frac{\Delta L}{\lambda} - \frac{\chi(z)}{2\pi} k \sin \theta_k \cos \phi_k \right) \\ &\times \left( \frac{\Delta L}{\lambda} - \frac{\chi(z)}{2\pi} k \sin \theta_k \sin \phi_k \right). \end{aligned} \quad (18)$$

As a last note, when computing numerical results in §VI, we substitute  $\phi_k$ -averaged version of this quantity (between 0 and  $\pi/2$  only, due to the four-fold symmetry

of the experimental setup of a square of dipoles) when computing the noise power, in order to account for the rotation of the baselines with respect to the modes. This average number density reads

$$\langle n_{\text{base}}(\vec{k}) \rangle_{\phi_k} = \left( \frac{\Delta L}{\lambda} \right)^2 - \frac{4}{\pi} \frac{\Delta L}{\lambda} \frac{\chi(z)}{2\pi} k \sin \theta_k + \left( \frac{\chi(z)}{2\pi} k \sin \theta_k \right)^2. \quad (19)$$

#### IV. QUADRATIC ESTIMATOR FORMALISM

In this Section, we derive an unbiased minimum-variance quadratic estimator for a cosmic magnetic field  $\vec{B}$  present in the IGM during the pre-reionization epoch. This formalism is applicable to tomographic data from future 21-cm surveys, and it is similar to that used in CMB analyses [33]. We assume that the field only evolves adiabatically, due to Hubble expansion,

$$B(z) = B_0(1+z)^2, \quad (20)$$

where  $B_0$  is its present-day value (its value in comoving units), and the corresponding estimator is denoted with a hat sign,  $\hat{B}_0$ .

We start by noting that the observed brightness temperature  $T(\vec{k})$  contains contributions from the noise  $T^N(\vec{k})$  (from the instrumental noise plus Galactic foreground emission) and the signal  $T^S(\vec{k})$ ,

$$T(\vec{k}) = T^N(\vec{k}) + T^S(\vec{k}), \quad (21)$$

where the “signal” may have contributions from previously discussed magnetic-field effects, as well as the null-case 21-cm emission (with no magnetic field present),  $T_0^S(\vec{k})$ . Note that we use the subscript “0” for functions evaluated at  $B_0 = 0$ . Signal temperature is proportional to the density fluctuation  $\delta$ , with transfer function  $G(\hat{\mathbf{k}})$  as the proportionality factor,

$$G(\hat{\mathbf{k}}) \equiv \frac{\partial T}{\partial \delta}(\hat{\mathbf{k}}, \delta = 0) \quad (22)$$

and

$$\begin{aligned} T^S(\vec{k}) &= G(\hat{\mathbf{k}})\delta(k), \\ T_0^S(\vec{k}) &= G_0(\hat{\mathbf{k}})\delta(k), \end{aligned} \quad (23)$$

where  $\hat{\mathbf{k}} = (\theta_k, \phi_k)$  is a unit vector in the direction of  $\vec{k}$ . Note that we do not write explicitly dependence of  $G$  on  $z$  and on cosmological parameters; furthermore, note that  $G$  is a function of the direction vector  $\hat{\mathbf{k}}$ , while the power spectrum  $P_\delta$  is a function of the magnitude  $k$ , in an isotropic universe. The explicit expression for the

transfer function is derived from Eq. (1),

$$\begin{aligned} G(\hat{\mathbf{k}}) &= \left( 1 - \frac{T_\gamma}{T_s} \right) x_{1s} \left( \frac{1+z}{10} \right)^{1/2} \\ &\times \left[ 26.4 \text{ mK} \left( 1 + (\hat{\mathbf{k}} \cdot \hat{\mathbf{n}})^2 \right) - 0.128 \text{ mK} \left( \frac{T_\gamma}{T_s} \right) \right. \\ &\times x_{1s} \left( \frac{1+z}{10} \right)^{1/2} \left\{ 2 \left( 1 + (\hat{\mathbf{k}} \cdot \hat{\mathbf{n}})^2 \right) \right. \\ &\left. \left. - \sum_m \frac{4\pi}{75} \frac{Y_{2m}(\hat{\mathbf{k}}) [Y_{2m}(\hat{\mathbf{n}})]^*}{1 + x_{\alpha,(2)} + x_{c,(2)} - imx_B} \right\} \right], \end{aligned} \quad (24)$$

for a reference frame where the magnetic field is along the  $z$ -axis. For simplicity of the expressions, we adopt the following notation

$$\begin{aligned} \frac{\partial T_0^S}{\partial B_0}(\vec{k}) &\equiv \delta(k) \frac{\partial G}{\partial B_0}(\hat{\mathbf{k}}, B_0 = 0), \\ \frac{\partial G_0}{\partial B_0}(\hat{\mathbf{k}}) &\equiv \frac{\partial G}{\partial B_0}(\hat{\mathbf{k}}, B_0 = 0), \end{aligned} \quad (25)$$

where  $\frac{\partial G_0}{\partial B_0} = \frac{\partial G_0}{\partial B} (1+z)^2$  for adiabatic evolution of the magnetic field.

The signal power spectrum in the absence of a magnetic field is given as

$$\begin{aligned} \langle T_0(\vec{k}) T_0^*(\vec{k}') \rangle &\equiv (2\pi)^3 \delta_D(\vec{k} - \vec{k}') P_0^S(\vec{k}) \\ &= (2\pi)^3 \delta_D(\vec{k} - \vec{k}') G_0^2(\hat{\mathbf{k}}) P_\delta(k), \end{aligned} \quad (26)$$

where

$$\langle \delta(\vec{k}) \delta^*(\vec{k}') \rangle \equiv (2\pi)^3 \delta_D(\vec{k} - \vec{k}') P_\delta(k). \quad (27)$$

The total measured null power spectrum is

$$P_{\text{null}}(\vec{k}) \equiv P^N(\vec{k}) + P_0^S(\vec{k}). \quad (28)$$

In §IV A, we first consider the case of a field uniform in the entire survey volume; this case is described by a single parameter,  $B_0$ . In §IV B, we move on to the case of a stochastic magnetic field, with a given power spectrum  $P_B(\vec{K})$  (where  $\vec{K}$  is the wavevector of a given mode of the field); in this case, the relevant parameter is the amplitude of this power spectrum,  $A_0^2$ . In both cases, we assume that there is a valid separation of scales: density-field modes in consideration must have much smaller wavelengths than the coherence scale of the magnetic field (or a given mode wavelength for the case of a stochastic magnetic field), and both length scales must be shorter than the size of the tomography survey.

##### A. Uniform field

In this Section, we derive an estimator  $\hat{B}_0$  for a comoving uniform magnetic field. We adopt the linear-theory approach and start with

$$T^S(\vec{k}) = T_0^S(\vec{k}) + B_0 \frac{\partial T_0^S}{\partial B_0}(\vec{k}), \quad (29)$$

where  $B_0$  is a small expansion parameter. The observable 2-point correlation function in Fourier space is then

$$\begin{aligned} \langle T(\vec{k})T^*(\vec{k}') \rangle &= P_{\text{null}}(\vec{k})(2\pi)^3\delta_D(\vec{k}-\vec{k}') \\ &+ \langle T_0^S(\vec{k})B_0\frac{\partial T_0^{S,*}}{\partial B_0}(\vec{k}') \rangle + \langle T_0^{S,*}(\vec{k}')B_0\frac{\partial T_0^S}{\partial B_0}(\vec{k}) \rangle \\ &= \left( P_{\text{null}}(\vec{k}) + 2B_0P_\delta(k)G_0(\hat{\mathbf{k}})\frac{\partial G_0}{\partial B_0}(\hat{\mathbf{k}}) \right) \\ &\quad \times (2\pi)^3\delta_D(\vec{k}-\vec{k}'), \end{aligned} \quad (30)$$

where we use the reality of  $G_0$  and  $\frac{\partial G_0}{\partial B_0}$ , assume that the signal and the noise are uncorrelated, and keep only terms linear in  $B_0$ . Since we observe only one universe, a proxy for the ensemble average in Eq. (30) is measurement of the product  $T(\vec{k})T^*(\vec{k}')$ . Thus, using Eq. (30), we get an estimate of  $B_0$  from a single temperature mode  $\vec{k}$ ,

$$\hat{B}_0^{\vec{k}} = \frac{\frac{1}{V}T(\vec{k})T^*(\vec{k}) - P_{\text{null}}(\vec{k})}{2P_\delta(k)G_0(\hat{\mathbf{k}})\frac{\partial G_0}{\partial B_0}(\hat{\mathbf{k}})}, \quad (31)$$

where we use the following properties of the Dirac delta function defined on a finite volume  $V$  of the survey

$$\begin{aligned} \delta_D(\vec{k}-\vec{k}') &= \frac{V}{(2\pi)^3}, \quad \text{for } \vec{k} = \vec{k}', \\ (2\pi)^3\delta_D(\vec{k}-\vec{k}') &\equiv \int e^{-i\vec{r}\cdot(\vec{k}-\vec{k}')} d\vec{r}, \end{aligned} \quad (32)$$

related to the Kronecker delta as

$$\delta_{\vec{k}\vec{k}'} = \frac{(2\pi)^3}{V}\delta_D(\vec{k}-\vec{k}'). \quad (33)$$

The estimator of Eq. (31) is unbiased, such that  $\langle \hat{B}_0^{\vec{k}} \rangle = 0$ . The covariance  $\langle \hat{B}_0^{\vec{k}}\hat{B}_0^{\vec{k}',*} \rangle$  of estimators derived from all measured temperature modes involves temperature-field 4-point correlation function with three Wick contractions, whose numerator reads

$$\begin{aligned} &\frac{1}{V^2}\langle T(\vec{k})T^*(\vec{k})T(\vec{k}')T^*(\vec{k}') \rangle + P_{\text{null}}(\vec{k})P_{\text{null}}(\vec{k}') \\ &- \frac{1}{V}P_{\text{null}}(\vec{k})\langle T(\vec{k}')T^*(\vec{k}') \rangle - \frac{1}{V}P_{\text{null}}(\vec{k}')\langle T(\vec{k})T^*(\vec{k}) \rangle \\ &= P_{\text{null}}(\vec{k})P_{\text{null}}(\vec{k}') \left[ \frac{(2\pi)^6}{V^2}\delta_D(\vec{k}-\vec{k})\delta_D(\vec{k}'-\vec{k}') \right. \\ &+ \frac{(2\pi)^6}{V^2}\delta_D(\vec{k}-\vec{k}')\delta_D(\vec{k}-\vec{k}') + \frac{(2\pi)^6}{V^2}\delta_D(\vec{k}+\vec{k}')\delta_D(\vec{k}+\vec{k}') \\ &\quad \left. - \frac{(2\pi)^3}{V}\delta_D(\vec{k}'-\vec{k}') - \frac{(2\pi)^3}{V}\delta_D(\vec{k}-\vec{k}) \right] \\ &= P_{\text{null}}(\vec{k})P_{\text{null}}(\vec{k}') \left( \delta_{\vec{k},\vec{k}'} + \delta_{\vec{k},-\vec{k}'} \right) \end{aligned} \quad (34)$$

where every ensemble average yielded one factor of  $V$ . Using the final expression in the above equation, we get

$$\langle \hat{B}_0^{\vec{k}}\hat{B}_0^{\vec{k}',*} \rangle = \frac{P_{\text{null}}^2(\vec{k}) \left( \delta_{\vec{k},\vec{k}'} + \delta_{\vec{k},-\vec{k}'} \right)}{4P_\delta(k)^2 \left[ G_0(\hat{\mathbf{k}})\frac{\partial G_0}{\partial B_0}(\hat{\mathbf{k}}) \right]^2}. \quad (35)$$

Estimators from all  $\vec{k}$ -modes can be combined with inverse-variance weighting to get

$$\hat{B}_0 = \frac{\sum_{\vec{k}} \frac{\hat{B}_0^{\vec{k}}}{\langle \hat{B}_0^{\vec{k}}\hat{B}_0^{\vec{k},*} \rangle}}{\sum_{\vec{k}} \frac{1}{\langle \hat{B}_0^{\vec{k}}\hat{B}_0^{\vec{k},*} \rangle}}. \quad (36)$$

Expanding this expression, we get the minimum-variance quadratic estimator for  $B_0$  obtained from all temperature-field modes observed at a given redshift,

$$\begin{aligned} \hat{B}_0 &= \sigma_{B_0}^2 \sum_{\vec{k}} \frac{\frac{1}{V}T(\vec{k})T^*(\vec{k}) - P_{\text{null}}(\vec{k})}{P_{\text{null}}^2(\vec{k})} \\ &\quad \times 2P_\delta(k)G_0(\hat{\mathbf{k}})\frac{\partial G_0}{\partial B_0}(\hat{\mathbf{k}}). \end{aligned} \quad (37)$$

Its variance is given by

$$\sigma_{B_0}^{-2} = \frac{1}{2} \sum_{\vec{k}} \left( \frac{2P_\delta(k)G_0(\hat{\mathbf{k}})\frac{\partial G_0}{\partial B_0}(\hat{\mathbf{k}})}{P_{\text{null}}(\vec{k})} \right)^2, \quad (38)$$

where the sums are unrestricted. Note that  $\hat{B}_0^{\vec{k}} = \hat{B}_0^{-\vec{k}}$ ; this follows from the reality condition on the temperature field,  $T(\vec{k}) = T^*(-\vec{k})$ , and from the isotropy of space in the null-assumption case,  $G_0(\hat{\mathbf{k}}) = G_0(-\hat{\mathbf{k}})$ . Thus, in order to avoid double-counting of modes, factor of  $1/2$  appears at the right-hand-side of Eq. (38).

## B. Stochastic field

We now examine the case where both the magnitude and the direction of the magnetic field are stochastic random variables, with spatial variation. Note that in this Section we do *not* assume a particular model for their power spectra. We use  $B_0$  to denote a component of the magnetic field along one of the three Cartesian-system axes, and  $\vec{r}$  to denote position vector in physical space, as before, and start with

$$T(\vec{r}) = T_0^S(\vec{r}) + B_0(\vec{r})\frac{\partial T_0^S}{\partial B_0}(\vec{r}), \quad (39)$$

where the subscripts and superscripts have the same meaning as before. In Fourier space, we now get

$$\begin{aligned} T(\vec{k}) &= T_0^S(\vec{k}) + \int d\vec{r} e^{-i\vec{k}\cdot\vec{r}} B_0(\vec{r})\frac{\partial T_0^S}{\partial B_0}(\vec{r}) \\ &= T_0^S(\vec{k}) + \frac{1}{(2\pi)^3} \int d\vec{k}_1 B_0(\vec{k}_1)\frac{\partial T_0^S}{\partial B_0}(\vec{k}-\vec{k}_1), \end{aligned} \quad (40)$$

where the last step uses the convolution theorem. The observable 2-point correlation function in Fourier space

then becomes

$$\begin{aligned} \langle T(\vec{k})T^*(\vec{k}') \rangle &= (2\pi)^3 \delta_D(\vec{k} - \vec{k}') P_{\text{null}}(\vec{k}) \\ &+ \left\langle T_0^{S,*}(\vec{k}') \frac{1}{(2\pi)^3} \int d\vec{k}_1 B_0(\vec{k}_1) \frac{\partial T_0^S}{\partial B_0}(\vec{k} - \vec{k}_1) \right\rangle \\ &+ \left\langle T_0^S(\vec{k}) \frac{1}{(2\pi)^3} \int d\vec{k}_1 B_0^*(\vec{k}_1) \left( \frac{\partial T_0^S}{\partial B_0}(\vec{k}' - \vec{k}_1) \right)^* \right\rangle, \end{aligned} \quad (41)$$

to first order in  $B_0$ . Note that, in this case, there is cross-mixing of different modes of the temperature field. From Eqs. (23), (25), and (27), we get

$$\begin{aligned} \langle T(\vec{k})T^*(\vec{k}') \rangle &= (2\pi)^3 \delta_D(\vec{k} - \vec{k}') P_{\text{null}}(\vec{k}) + B_0(\vec{k} - \vec{k}') \\ &\times \left[ P_\delta(k') G_0^*(\hat{\mathbf{k}}') \frac{\partial G_0}{\partial B_0}(\hat{\mathbf{k}}') + P_\delta(k) G_0(\hat{\mathbf{k}}) \frac{\partial G_0^*}{\partial B_0}(\hat{\mathbf{k}}) \right], \end{aligned} \quad (42)$$

where we also use the reality condition  $B_0^*(-\vec{K}) = B_0(\vec{K})$ . In analogy to the procedure of §IV A, we estimate  $B_0(\vec{K})$  from  $\vec{k}\vec{k}'$  pair of modes that satisfy  $\vec{K} = \vec{k} - \vec{k}'$  as

$$\hat{B}_0^{\vec{k}\vec{k}'}(\vec{K}) = \frac{T(\vec{k})T^*(\vec{k}')}{P_\delta(k') G_0^*(\hat{\mathbf{k}}') \frac{\partial G_0}{\partial B_0}(\hat{\mathbf{k}}') + P_\delta(k) G_0(\hat{\mathbf{k}}) \frac{\partial G_0^*}{\partial B_0}(\hat{\mathbf{k}})}, \quad (43)$$

where we only focus on terms  $\vec{K} \neq 0$  ( $\vec{k} \neq \vec{k}'$ ). The variance  $\langle \hat{B}_0^{\vec{k}\vec{k}'}(\vec{K}) \left( \hat{B}_0^{\vec{k}\vec{k}'}(\vec{K}') \right)^* \rangle$  of this estimator (under the null assumption) can be evaluated using the above expression. Furthermore, the full estimator for  $B_0(\vec{K})$  from all available temperature modes is obtained by combining individual  $\hat{B}_0^{\vec{k}\vec{k}'}(\vec{K})$  estimates with inverse-variance weights, and with appropriate normalization, in complete analogy to the uniform-field case. For the purpose of detectability analysis, we are interested in the variance of the minimum-variance estimator, or equivalently, the noise power spectrum of  $\hat{B}_0$ , which reads

$$\begin{aligned} (2\pi)^3 \delta_D(\vec{K} - \vec{K}') P_{B_0}^N(\vec{K}) &\equiv \langle \hat{B}_0(\vec{K}) \hat{B}_0(\vec{K}')^* \rangle \\ &= \left( \sum_{\vec{k}} \frac{\left( P_\delta(k') G_0^*(\hat{\mathbf{k}}') \frac{\partial G_0}{\partial B_0}(\hat{\mathbf{k}}') + P_\delta(k) G_0(\hat{\mathbf{k}}) \frac{\partial G_0^*}{\partial B_0}(\hat{\mathbf{k}}) \right)^2}{2V^2 P_{\text{null}}(\vec{k}) P_{\text{null}}(\vec{k}')} \right)^{-1}, \end{aligned} \quad (44)$$

with the restriction  $\vec{K} = \vec{k} - \vec{k}'$ . Factor of 2 in the denominator corrects for double-counting mode pairs since  $\hat{B}_0^{\vec{k}\vec{k}'}(\vec{K}) = \left( \hat{B}_0^{-\vec{k}-\vec{k}'}(\vec{K}) \right)^*$ , and the sum is unconstrained. If we only consider diagonal terms  $\vec{K} = \vec{K}'$ , then the left-hand-side becomes equal to  $V P_{B_0}^N(\vec{K})$ . The

explicit expression for the noise power spectrum is then

$$P_{B_0}^N(\vec{K}) = \left( \sum_{\vec{k}} \frac{\left( P_\delta(k') G_0^*(\hat{\mathbf{k}}') \frac{\partial G_0}{\partial B_0}(\hat{\mathbf{k}}') + P_\delta(k) G_0(\hat{\mathbf{k}}) \frac{\partial G_0^*}{\partial B_0}(\hat{\mathbf{k}}) \right)^2}{2V P_{\text{null}}(\vec{k}) P_{\text{null}}(\vec{k}')} \right)^{-1}. \quad (45)$$

Only the components of the magnetic field in the plane of the sky have an effect of the observed brightness temperature, and so Eq. (45) can be used to evaluate the noise power spectrum for either one of those two (uncorrelated) components. The noise in the direction along the line of sight can be considered infinite. Finally, note that we can construct a similar estimator for the direction of the magnetic field, in a given patch of the sky. However, in this work we only focus on the magnitude of the field and ignore considerations with regard to its direction.

## V. FISHER ANALYSIS

We now use the key results of §IV to evaluate sensitivity of future tomographic 21-cm surveys to detecting presence of magnetic fields in high-redshift IGM. In §V A, we derive the expression for sensitivity to a field uniform in the entire survey volume. We start with the unsaturated case, and consider the limit where the field (in the classical picture) produces less than 1 radian of precession at all redshifts of interest, and then move on to the saturated (strong field) limit. In §V B, we derive the expression for sensitivity to detecting a stochastic magnetic field described by a specific, scale-invariant, power spectrum.

### A. Uniform field case

Eq. (38) provides an expression for evaluating  $1\sigma$  sensitivity to measuring a uniform  $B_0$  at a given redshift. The total sensitivity of a tomography survey over a range of redshifts is given by integrating over the available redshift range,

$$\begin{aligned} \sigma_{B_0, \text{tot}}^{-2} &= \frac{1}{2} \int dV(z) \frac{k^2 dk d\phi_k \sin \theta_k d\theta_k}{(2\pi)^3} \\ &\times \left( \frac{2P_\delta(k, z) G_0(\theta_k, \phi_k, z) \frac{\partial G_0}{\partial B_0}(\theta_k, \phi_k, z)}{P^N(k, \theta_k, z) + P_\delta(k, z) G_0^2(\theta_k, \phi_k, z)} \right)^2, \end{aligned} \quad (46)$$

where we transitioned from a sum over  $\vec{k}$  modes to an integral, using  $\sum_{\vec{k}} \rightarrow V \int d\vec{k}/(2\pi)^3$ . The integral is performed over the (comoving) volume of the survey of angular size  $\Omega_{\text{survey}}$  (in steradians) at a given redshift, such that the volume element reads

$$dV = \frac{c}{H(z)} \chi^2(z) \Omega_{\text{survey}} dz. \quad (47)$$

The integration limits are:  $\phi_k \in [0, 2\pi]$ ;  $\theta_k \in [0, \pi]$ ; and  $k \in [2\pi u_{\min}/(d_A \sin \theta_k), 2\pi u_{\max}/(d_A \sin \theta_k)]$ , where  $u_{\min, \max} = \frac{L_{\min, \max}}{\lambda}$  correspond to the maximum and minimum baseline,  $L_{\min}$  and  $L_{\max}$ , respectively. If the survey area is big enough that the flat-sky approximation breaks down,  $\sigma_{B_0}^{-2}$  can be computed on small (approximately flat) patch of size  $\Omega_{\text{patch}}$  and centered on the line of sight, and then corrected to account for the total survey volume<sup>2</sup>. The corrected sensitivity can be evaluated as

$$\begin{aligned} \sigma_{B_0, \text{corr}}^{-2} &= \frac{\sigma_{B_0, \text{patch}}^{-2}}{\Omega_{\text{patch}}} \int_0^{\theta_{\text{survey}}} \int_0^{2\pi} \cos^2 \theta d\theta d\phi \\ &= \frac{\pi \sigma_{B_0, \text{patch}}^{-2}}{\Omega_{\text{patch}}} (\theta_{\text{survey}} + \cos \theta_{\text{survey}} \sin \theta_{\text{survey}}). \end{aligned} \quad (48)$$

So far, we have only focused on the regime of the weak magnetic field. Let us now consider the case where the field is strong enough that the precession period is comparable or shorter than the lifetime of the excited atomic state—saturated regime. In this case, the brightness-temperature 2-point correlation functions still capture the presence of the field (as illustrated in Figure 2), but they lose information about its magnitude and may only be used to determine the lower limit of the field strength. Ability to distinguish saturated case from zero magnetic field becomes a relevant measure of survey sensitivity in this scenario.

We now write the signal power spectrum as a sum of contributions from  $B_0 = 0$  and  $B_0 \rightarrow \infty$  scenarios,

$$P^S(\vec{k}) = (1 - \xi)P^S(\vec{k}, B = 0) + \xi P^S(\vec{k}, B \rightarrow \infty), \quad (49)$$

and perform the standard Fisher analysis to evaluate sensitivity to recovering parameter  $\xi$ ,

$$\sigma_\xi^{-2} = \int dV(z) \frac{d\vec{k}}{(2\pi)^3} \left( \frac{\partial P^S(\vec{k})}{\partial \xi} \right)^2, \quad (50)$$

where

$$\frac{\partial P^S(\vec{k})}{\partial \xi} = P^S(\vec{k}, B \rightarrow \infty) - P^S(\vec{k}, B = 0) \quad (51)$$

involves the following limit of the transfer function, derived from Eq. (24),

$$\begin{aligned} G(\hat{\mathbf{k}}, B \rightarrow \infty) &= \left(1 - \frac{T_\gamma}{T_s}\right) x_{1s} \left(\frac{1+z}{10}\right)^{1/2} \\ &\times \left[ 26.4 \text{ mK} \left(1 + (\hat{\mathbf{k}} \cdot \hat{\mathbf{n}})^2\right) - 0.128 \text{ mK} \left(\frac{T_\gamma}{T_s}\right) \right] \\ &\times x_{1s} \left(\frac{1+z}{10}\right)^{1/2} \left\{ 2 + 2(\hat{\mathbf{k}} \cdot \hat{\mathbf{n}})^2 - \frac{1}{60} \frac{1 - 3\cos^2 \theta_k}{1 + x_{\alpha, (2)} + x_{c, (2)}} \right\}, \end{aligned} \quad (52)$$

in the reference frame where the magnetic field is along the  $z$  axis, and the line-of-sight direction is perpendicular to it; when using this expression to derive numerical results in the following Section, we are only interested in this configuration, since we only evaluate detectability of the components of  $\vec{B}$  in the plane of the sky. We interpret  $\sigma_\xi$  as  $1\sigma$  sensitivity to *detecting* presence of a strong magnetic field.

## B. Stochastic field case

Using Eq. (45) and transitioning from a sum to the integral (like in §V A), we get the following expression for the noise power spectrum of one of the components  $B_{0,i}$  of the magnetic field in the plane of the sky,

$$\begin{aligned} \left(P_{B_{0,i}}^N(\vec{K})\right)^{-1} &= \int k^2 dk \sin \theta_k d\theta_k d\phi_k \\ &\times \frac{\left(P_\delta(k') G_0^*(\hat{\mathbf{k}}') \frac{\partial G_0}{\partial B_i}(\hat{\mathbf{k}}') + P_\delta(k) G_0(\hat{\mathbf{k}}) \frac{\partial G_0^*}{\partial B_i}(\hat{\mathbf{k}})\right)^2}{2(2\pi)^3 P_{\text{null}}(\vec{k}) P_{\text{null}}(\vec{k}')}, \end{aligned} \quad (53)$$

where  $\vec{k}' = \vec{K} - \vec{k}$  and the above expression is evaluated at a particular redshift. To compute signal-to-noise ratio (SNR) for measuring the amplitude of a stochastic-field power spectrum, at a given redshift, we start with the general expression

$$\text{SNR}^2 = \frac{1}{2} \text{Tr} (N^{-1} S N^{-1} S), \quad (54)$$

where  $S$  and  $N$  stand for the signal and noise matrices, respectively, and  $\text{Tr}$  is the trace of the matrix. In our case, these are  $3N_{\text{voxels}} \times 3N_{\text{voxels}}$  matrices (there are 3 components of the magnetic field and  $N_{\text{voxels}}$  voxels). In the null case, voxels are independent and the noise matrix is diagonal. Voxel-noise variance for measuring a single mode is given by  $P_{B_{0,i}}^N(\vec{K}, z)/V_{\text{voxel}}(z)$ , where  $V_{\text{voxel}}$  is voxel volume. Summing over all voxels and components of the magnetic field with inverse-variance weights gives

$$\begin{aligned} \text{SNR}^2(z) &= \frac{1}{2} \sum_{i\alpha, j\beta} \frac{S_{i\alpha, j\beta}^2}{P_{B_{0,i}}^N(\vec{K}, z) P_{B_{0,j}}^N(\vec{K}, z)} V_{\text{voxel}}^2 \\ &= \frac{1}{2} \sum_{ij} \int d\vec{r}_\alpha \int d\vec{r}_\beta \frac{\langle B_{0,i}(\vec{r}_\alpha) B_{0,j}(\vec{r}_\beta) \rangle^2}{P_{B_{0,i}}^N(\vec{K}, z) P_{B_{0,j}}^N(\vec{K}, z)}, \end{aligned} \quad (55)$$

at a given redshift. Greek indices label individual voxels and, as before, Roman indices denote field components;  $\vec{r}_{\alpha/\beta}$  represents spatial position of a given voxel.

To simplify further calculations, we now focus on a particular class of magnetic-field models where most of the power is on largest scales (small  $\vec{K}$ ). In this (squeezed) limit,  $\vec{K} \ll \vec{k}$  and thus  $\vec{k} \approx \vec{k}'$ , such that Eq. (53) reduces to the white noise (becomes independent on  $\vec{K}$ ). A model for the power spectrum is defined through

$$(2\pi)^3 \delta_D(\vec{K} - \vec{K}') P_{B_{0,i} B_{0,j}}(\vec{K}) \equiv \langle B_{0,i}^*(\vec{K}) B_{0,j}(\vec{K}') \rangle, \quad (56)$$

<sup>2</sup> This accounts for the change in the angle that a uniform magnetic field makes with a line of sight, as the line of sight “scans” through the survey area.



which relates to the variance in the transverse component  $P_{B\perp}(\vec{K})$  as

$$P_{B_{0,i}B_{0,j}}(\vec{K}) = (\delta_{ij} - \hat{K}_i \hat{K}_j) P_{B\perp}(\vec{K}), \quad (57)$$

where  $\hat{K}_{i/j}$  is a unit vector along the direction of  $i/j$  component. In the rest of this discussion, for concreteness, we consider a scale-invariant (SI) power spectrum,

$$P_{B\perp}(\vec{K}) = A_0^2 / K^3. \quad (58)$$

Here, the amplitude  $A_0$  is a free parameter of the model (in units of Gauss). Furthermore, if homogeneity and isotropy are satisfied, the integrand in Eq. (55) only depends on the separation vector  $\vec{s} \equiv \vec{r}_\beta - \vec{r}_\alpha$ . Using this, and the squeezed limit assumption, gives<sup>3</sup>

$$\begin{aligned} \text{SNR}^2(z) &= \frac{1}{2} \sum_{ij} \frac{dV_{\text{patch}}}{(P_{B_{0,i}}^N(z))^2} \int d\vec{s} \langle B_{0,i}(\vec{r}_\beta - \vec{s}) B_{0,j}(\vec{r}_\beta) \rangle^2 \\ &= \frac{1}{2(2\pi)^3} \sum_{ij} \frac{dV_{\text{patch}}}{(P_{B_{0,i}}^N(z))^2} \int d\vec{K} \left( P_{B_{0,i}B_{0,j}}(\vec{K}) \right)^2, \end{aligned} \quad (59)$$

where  $dV_{\text{patch}}$  is the volume of a redshift-slice patch defined in Eq. (47). Substituting Eq. (58), and integrating over redshifts, total SNR is given by

$$\begin{aligned} \text{SNR}^2 &= \frac{A_0^4}{2(2\pi)^3} \int_{z_{\min}}^{z_{\max}} \frac{dV_{\text{patch}}}{(P_{B_{0,i}}^N(z))^2} \int_0^\pi \sin \theta d\theta \\ &\quad \int_0^{2\pi} d\phi \int_{K_{\min}(z,\theta,\phi)}^{K_{\max}(z,\theta,\phi)} \frac{dK}{K^4} \sum_{ij \in \{xx, xy, yx, yy\}} (\delta_{ij} - \hat{K}_i \hat{K}_j)^2, \end{aligned} \quad (60)$$

where  $x$  and  $y$  denote components in the plane of the sky, and

$$\hat{K}_x = \sin \theta \sin \phi, \quad \hat{K}_y = \sin \theta \cos \phi. \quad (61)$$

The sum in the above expression reduces to

$$\sum_{ij \in \{xx, xy, yx, yy\}} (\delta_{ij} - \hat{K}_i \hat{K}_j)^2 = 2 \cos^2 \theta + \sin^4 \theta. \quad (62)$$

Substituting this into Eq. (60) and integrating over  $K, \theta, \phi$  gives

$$\text{SNR}^2 = \frac{A_0^4}{10\pi^2} \int_{z_{\min}}^{z_{\max}} \frac{dV_{\text{patch}}}{(P_{B_{0,i}}^N(z))^2} \left( \frac{1}{K_{\min}^3} - \frac{1}{K_{\max}^3} \right). \quad (63)$$

Finally, from the above expression,  $1\sigma$  sensitivity to measuring  $A_0^2$  is given by

$$\sigma_{A_0^2}^2 = \left[ \frac{1}{10\pi^2} \int_{z_{\min}}^{z_{\max}} \frac{dV_{\text{patch}}}{(P_{B_{0,i}}^N(z))^2} \left( \frac{1}{K_{\min}^3} - \frac{1}{K_{\max}^3} \right) \right]^{-1}. \quad (64)$$

Note at the end that, for our choice of the SI power spectrum, the choice of  $K_{\max}$  does not matter, while we choose  $K_{\min}$  to match the survey size at a given redshift.

<sup>3</sup> In the last step, we used  $\int d\vec{s} |f(\vec{s})|^2 = \int \frac{d\vec{K}}{(2\pi)^3} |\tilde{f}(\vec{K})|^2$ , which holds for an arbitrary function  $f$  and its Fourier transform  $\tilde{f}$ .

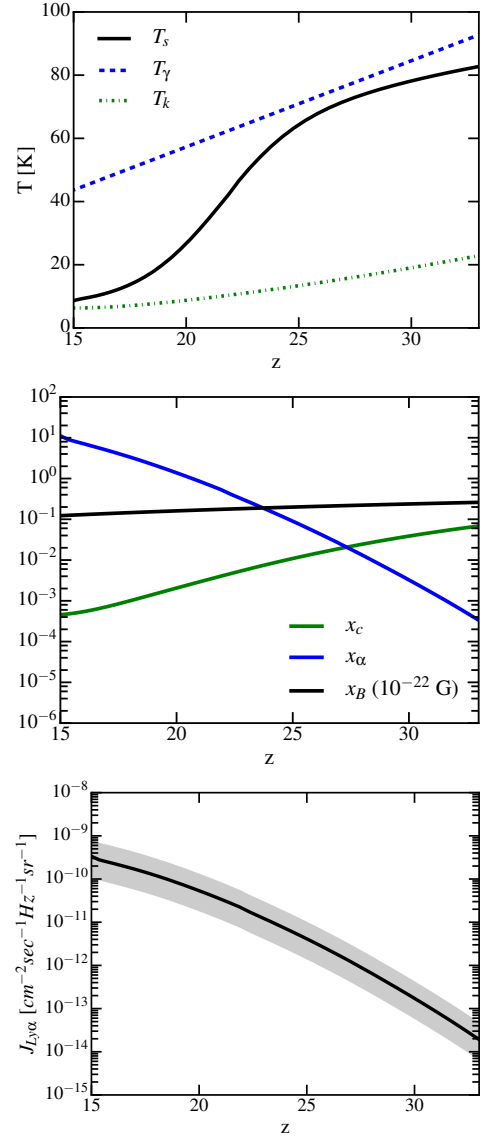


Figure 3. Inputs used for the sensitivity calculation, computed for standard cosmology using 21CMFAST code. Top panel: fiducial spin, kinetic, and CMB temperatures. Middle panel: fiducial models for quantities that parametrize the rate of depolarization of the ground state by optical pumping and atomic collisions, and the rate of magnetic precession for a representative value of the magnetic field. Bottom panel: Lyman- $\alpha$  flux model; fiducial choice is shown with a solid line, while the gray band captures the level of modeling uncertainty (it spans of the “extremal” input models used to test sensitivity of our calculation to this uncertainty, as discussed in the text).

## VI. RESULTS

We now proceed to numerically evaluate the sensitivity of 21-cm tomography to magnetic fields during the pre-reionization epoch, using the formalism from previous two Sections. For this purpose, we only focus on

one type of experimental setup—an array of dipole antennas arranged in a compact grid, such as implemented in HERA, for example. The motivation for this choice is that such a configuration maximizes sensitivity to recovering the power spectrum of the cosmological 21-cm signal [29, 32]. We consider an array with a collecting area of  $(\Delta L \text{ km})^2$ , where  $\Delta L$  is taken to be the maximal baseline separation.

Calculation of the observation time  $t_1$  (appearing in the expression for the noise in Eq. (13)), for a given total survey duration  $t_{\text{obs}}$ , depends on the type of the experiment. For a radio dish with a beam of solid angle  $\Omega_{\text{beam}} = \lambda^2/A_e$  that is much smaller than the survey size  $\Omega_{\text{survey}}$ , the telescope scans the sky one beamwidth at a time. In that case,  $t_1$  is the total time spent observing one  $(u, v)$  element  $t_1 = t_{\text{obs}}\Omega_{\text{survey}}/\Omega_{\text{beam}}$ . However, in the case of an array of dipoles we are considering here, the beam size is greater than (or equal to) the survey size, and  $t_1 = t_{\text{obs}}$ . We do not explicitly account for the fact that any given patch of the sky is only visible for a part of the day from a given location; therefore,  $t_{\text{obs}}$  we substitute in the noise calculation is shorter than the wall-clock duration of the survey by a factor of a few. To derive numerical results, we assume  $\Omega_{\text{survey}} = 1\text{sr}$ , and the wall-clock survey duration of about 2 years (corresponding to  $t_{\text{obs}} = 1 \text{ year}$ ).

For the sky temperature that enters the noise power spectrum in Eq. (13), we assume a simple model of Galactic synchrotron emission from Ref. [34],

$$T_{\text{sky}} = 60 \left( \frac{21}{100} (1+z) \right)^{2.55} [\text{K}]. \quad (65)$$

Other ingredients entering our sensitivity calculation are the mean Lyman- $\alpha$  flux  $J_{\text{Ly}\alpha}(z)$ , the spin  $T_s$  and the kinetic  $T_k$  temperatures of the IGM, and the CMB temperature  $T_\gamma$ , all functions of redshift. We obtain all of these quantities from 21CMFAST code [35]. As input to 21CMFAST, we used standard cosmology ( $H_0 = 67 \text{ km s}^{-1} \text{ Mpc}^{-1}$ ,  $\Omega_m = 0.32$ ,  $\Omega_K = 0$ ,  $n_s = 0.96$ ,  $\sigma_8 = 0.83$ ,  $w = -1$ ) consistent with Planck measurements [36], set the stellar population responsible for early heating to Population III, and kept all other input parameters at their default values, with the exception of the star formation efficiency,  $F_{\text{STAR}}$ . For our fiducial calculation, we choose the value of  $F_{\text{STAR}} = 0.0075$ , corresponding to the solid lines in Figure 3. The top panel shows quantities (discussed in Paper I) that parametrize the rates of depolarization of the ground state by optical pumping and atomic collisions, and the rate of magnetic precession. The middle panel shows the relevant gas and CMB temperatures. The bottom panel shows  $J_{\text{Ly}\alpha}(z)$ , where the solid line, as before, corresponds to the fiducial choice of parameters, while the gray band of “uncertainty” around this curve corresponds to  $F_{\text{STAR}} = 0.0025$  and  $F_{\text{STAR}} = 0.01875$ . The fiducial choice produces a match of the flux to the models in Ref. [37] at  $z = 15$ , while the gray band is chosen to roughly capture the level of the uncertainty in the flux modeling at high redshifts

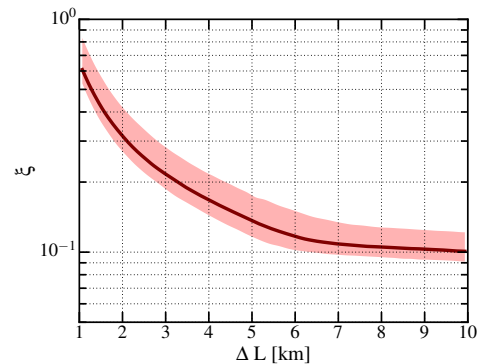


Figure 4. Projected sensitivity to detecting a magnetic field in the saturated regime, as a function of the maximum baseline (or, equivalently, of the total collecting area,  $(\Delta L)^2$ ), assuming a survey size of 1 sr and survey duration of 2 years. The parameter on the  $y$  axis characterizes the distinction between the case of no magnetic field ( $\xi = 0$ ) and the presence of a strong field ( $\xi = 1$ ). Smaller values here (for larger maximum-baseline values shown on the  $x$  axis) correspond to more precise recovery of  $\xi$  and a more confident distinction between those two regimes. The light-colored band around the solid line corresponds to the Lyman- $\alpha$  model flux uncertainty, represented with a gray band in Figure 3.

(given the lack of direct observation at high  $z$ ). We use these extreme models (corresponding to the bounds of the gray band in this Figure) to test sensitivity of our key results to the uncertainty in the evolution of the Lyman- $\alpha$  flux and other input parameters (note that we do not plot corresponding uncertainty bands on the other two panels, simply to avoid clutter; but we use them consistently in our sensitivity calculation). We assume that the redshifts available for this analysis are between 15 and 35. As we will see from Figure 6 (discussed in more detail below), most of the sensitivity comes from redshifts where the spin temperature starts decoupling from the CMB; for our fiducial case, it is around  $z \sim 21$ .

Figures 4 and 5 show the key results: the projected sensitivity of tomographic surveys as a function of the maximum baseline  $\Delta L$  (where different baselines may correspond to different stages of a single experiment). Figure 4 shows  $1\sigma$  sensitivity to parameter  $\xi$  of Eq. (49), which quantifies the distinction between the case of no magnetic field and the case where the field is strong and the signal is in the saturated regime. The value of this parameter is, by definition, bound between 0 and 1, where 0 represents the case of no magnetic field, and 1 represents the saturated case. In this Figure, the solid line represents the fiducial calculation, while the light-colored band around it corresponds to the uncertainty band of inputs shown in Figure 3. The fiducial result implies that an array with one kilometer squared of collecting area can achieve  $1\sigma$  detection threshold, which can be interpreted as follows. If a survey were to measure  $\xi \neq 0$ , that would be a  $1\sigma$  detection of a lower bound on a uniform magnetic field in the entire survey volume. The value of the

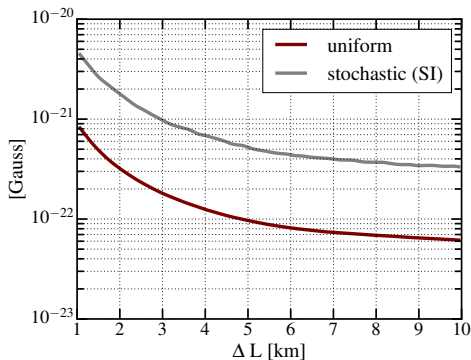


Figure 5. Projected  $1\sigma$  sensitivity to detecting a uniform (lower red line) and a stochastic (upper gray line) magnetic field, as a function of maximum baseline  $\Delta L$  (the collecting area of the array is given as  $(\Delta L)^2$ ). For the stochastic field, we assume a scale-invariant (SI) power spectrum, and show the root-mean-square variation per  $\log K$ , given by  $A_0/\pi$ , where  $A_0^2$  is the amplitude of the power in a transverse component), as a function of maximum array baseline, assuming a survey size of 1 sr, and for survey duration of 2 years.

lower bound as a function of redshift would correspond to the saturation ceiling at that redshift, which can be roughly evaluated from the condition that the depolarization rates through standard channels equal the rate of magnetic precession,  $x_B = 1 + x_{\alpha,(2)} + x_{c,(2)}$ . The ceiling is depicted with a dashed line in Figure 6, and it corresponds to  $|\vec{B}| \sim 2 \times 10^{-21}$  Gauss (comoving) at  $z = 20$ , for example. On the other hand, if a survey were to report a null result, it would rule out such a magnetic field, at the same confidence level. In that case, we can compute an upper bound on the strength of the magnetic field components in the plane of the sky, as discussed in the following.

We obtain results in Figure 5 by evaluating the expressions of Eqs. (46) and (63). This Figure shows a projected  $1\sigma$  upper bound that can be placed on the value of the magnetic field, in case of no detection with an array of given size. The result is shown for both the uniform field (lower solid red line), and for the amplitude of a stochastic field (upper gray line) with a scale-independent power spectrum. While the numerical calculation assumed that the brightness temperature is a linear function of the field strength, this assumption is not guaranteed to hold—it breaks down in the saturation limit, as discussed above and in §II. So, this Figure is only valid if  $\xi = 0$ .

In order to understand how the projected constraints (sensitivities) presented in Figure 5 compare to the saturation ceiling at the redshifts we consider, Figure 6 shows a comparison between the saturation ceiling and the values of the  $z$ -dependent integrands of Eq. (46) (plotted for several array sizes). We can now see that the sensitivity to the uniform field corresponding to all array sizes in consideration is below the saturation regime for the redshifts where most of the SNR comes from:  $z \sim 21$  (the minima of these curves). This gives us confidence that

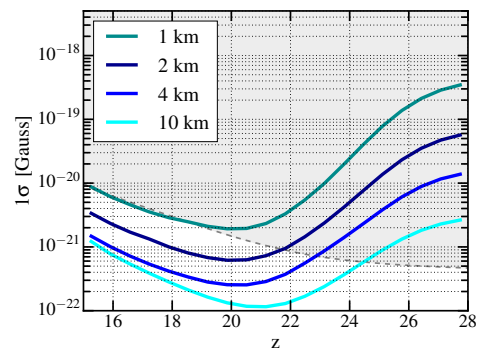


Figure 6. Saturation regime is shown as a shaded gray area above the dashed curve. Integrand of Eq. (46) (inverse square root of it) is shown as a function of redshift, for several maximum—baseline lengths. When the colored curves are below the saturation limit around their minima, the analysis assuming unsaturated regime is valid.

the results for the uniform field in Figure 5 are indeed valid, and the linear theory holds in the given regime (the transfer function is a linear function of the field strength). For the stochastic case, however, it is likely that a factor of a few larger array sizes are needed to achieve sensitivity that is below the saturation limit at relevant redshifts. It is also important to note here that the calculation of the saturation ceiling presented in this Figure is quite conservative, where in reality linear approximation should hold well until the field reaches a value that is a few times above this level.

## VII. SUMMARY AND CONCLUSIONS

In Paper I of this series, we proposed a new method to detect extremely weak magnetic fields in the IGM during the Dark Ages, using 21-cm tomography. In this paper, Paper II, we investigated sensitivity of this method with future 21-cm tomography surveys. For this purpose, we developed a minimum-variance-estimator formalism that uses measurements of the 21-cm brightness temperature to probe magnetic fields prior to the epoch of reionization.

The main results are in Figures 4 and 5. Their implication is that a radio array in a compact-grid configuration with a square kilometer collecting area has the sensitivity necessary to put an upper bound of  $10^{-21}$  Gauss comoving on a uniform magnetic fields at high redshifts. The case of a stochastic field is more challenging (by a factor of a few in the case of a scale-invariant power spectrum), and measuring the spectral shape of such a field would require even larger arrays to achieve. In this analysis, we took into account the noise component arising from the presence of large Galactic foreground signal, but we ignored more other effects (such as, for example, frequency dependence of the beams, etc.) which may further complicate reconstruction of such signal and should be taken

into account in a detailed analyses for figures of merit for future experiments. Finally, we note that gravitational lensing of the 21-cm signal by the intervening large scale structure can in principle present a contaminant for the magnetic field measurement. In Appendix B, we examine this possibility and show that the contamination is negligible for arrays with coverage areas considered in this work.

A kilometer squared of collecting area corresponds to a radio-array size planned for the next stages of some of the current reionization-epoch experiments (in terms of the number of antennas, compare to HERA and to the SKA [27], for example). The number of mode measurements required for placing a meaningful upper limit on such early-time magnetic fields using our method does not supersede computational demands for the next-generation experiments and is thus achievable in the coming future. Finally, it is also worth emphasizing again that the main limitation to the sensitivity is the fact that the effects we considered are based on a two-scattering process—as soon as quality of the 21-cm statistics reaches the level necessary to probe second-order processes, the effect of magnetic precession we discussed in this series of papers will open up an “*in situ*” probe of minuscule (and possibly primordial) magnetic fields at high redshift with unprecedented precision.

## ACKNOWLEDGMENTS

VG gratefully acknowledges the support from the W. M. Keck Foundation Fund at the Institute for Advanced Study. TV gratefully acknowledges support from the Schmidt Fellowship and the Fund for Memberships in Natural Sciences at the Institute for Advanced Study. AM, CH, and AO are supported by the U.S. Department of Energy, the David & Lucile Packard Foundation, and the Simons Foundation. XF is supported by the Simons Foundation. The authors thank Juna Kollmeier and Francesco Haardt for a useful conversation on Lyman- $\alpha$  flux evolution. Illustrations in Figure 2 made use of HEALPix [38] software package<sup>4</sup>.

## Appendix A: Visibility variance

Here we derive the variance of the visibility for an interferometric array of two antennas separated by a baseline  $\vec{b} = (b_x, b_y)$ , each with an effective collecting area  $A_e$ , observing a single element in the  $uv$  plane for time duration  $t_1$ , with total bandwidth  $\Delta\nu = \nu_{\max} - \nu_{\min}$ . A schematic of this setup is shown in Figure 7. Modes with frequencies that differ by less than  $1/t_1$  cannot be distinguished,

and modes with frequencies in each interval  $1/t_1$  are collapsed into a discrete mode with frequency  $\nu_n = n/t_1$ , where  $n \in Z$ . Thus, the number of measured (discrete) frequencies is  $N_\nu = t_1 \Delta\nu$ . Electric field induced in a single antenna is

$$E(t) = \sum_n^{N_\nu} \tilde{E}(\nu_n) e^{2\pi i \nu_n t}, \quad (\text{A1})$$

while the quantity an interferometer measures is the correlation coefficient between the electric field  $E_i$  in one and the electric field  $E_j$  in the other antenna as a function of frequency,

$$\rho_{ij}(\nu) \equiv \frac{\langle \tilde{E}_i^*(\nu) \tilde{E}_j(\nu) \rangle}{\sqrt{\langle |\tilde{E}_i(\nu)|^2 \rangle \langle |\tilde{E}_j(\nu)|^2 \rangle}}. \quad (\text{A2})$$

Let us now assume that

$$\langle \tilde{E}_i^*(\nu_n) \tilde{E}_j(\nu_m) \rangle = \sigma(\nu)^2 \delta_{mn}, \quad (\text{A3})$$

In the following, for clarity, we omit explicitly writing the dependence on  $\nu$ . The real (or imaginary) part of  $\rho$  has the following variance

$$\text{var}(\text{Re}[\rho_{ij}]) \frac{1}{2N_\nu} = \frac{1}{2t_1 \Delta\nu}. \quad (\text{A4})$$

Before continuing, let us take a brief digression to show that the above formula implicitly assumes that the electric fields in the two antennas have a very weak correlation,  $\rho \ll 1$ . Consider two random Gaussian variables,  $x$  and  $y$ , both with zero mean values, where  $\text{var}(x) \equiv \langle (x - \langle x \rangle)^2 \rangle = \langle x^2 \rangle - \langle x \rangle^2 = \langle x^2 \rangle$ , and similarly for  $y$ . Their correlation coefficient is  $\rho \equiv \frac{\langle xy \rangle}{\sqrt{\langle x^2 \rangle \langle y^2 \rangle}}$ . In this case, the following is true

$$\begin{aligned} \text{var}(xy) &= \langle x^2 y^2 \rangle - \langle xy \rangle^2 = \langle x^2 \rangle \langle y^2 \rangle + \langle xy \rangle^2 \\ &= \langle x^2 \rangle \langle y^2 \rangle + \rho^2 \langle x^2 \rangle \langle y^2 \rangle = \text{var}(x) \text{var}(y) (1 + \rho^2), \end{aligned} \quad (\text{A5})$$

so that when  $\rho$  is small,  $\text{var}(xy) = \text{var}(x) \text{var}(y)$ , which was assumed in the first equality of Eq. (A4).

Resuming the derivation, if different frequencies are uncorrelated, the result of Eq. (A4) implies

$$\langle |\rho_{ij}(\nu)|^2 \rangle = \frac{1}{t_1 \Delta\nu}. \quad (\text{A6})$$

The final step requires a relation between intensity in the sky  $\mathcal{I}(\theta_x, \theta_y, \nu)$  (within the beam of the solid angle  $\Omega_{\text{beam}}$ , centered on the direction  $\hat{\mathbf{n}} = (\theta_x, \theta_y)$ ) and the electric fields measured in the two antennas,

$$\begin{aligned} \langle \tilde{E}_i^*(\nu) \tilde{E}_j(\nu) \rangle &\propto \int_{\Omega_{\text{beam}}} d\theta_x d\theta_y \mathcal{I}(\theta_x, \theta_y, \nu) \\ &\times e^{i \frac{2\pi\nu}{c} (b_x \theta_x + b_y \theta_y)} R(\theta_x, \theta_y), \end{aligned} \quad (\text{A7})$$

where  $R(\theta_x, \theta_y)$  is the antenna response function (the shape of the beam in the sky), which we will assume to

<sup>4</sup> <http://healpix.sf.net>; <https://github.com/healpy/healpy>

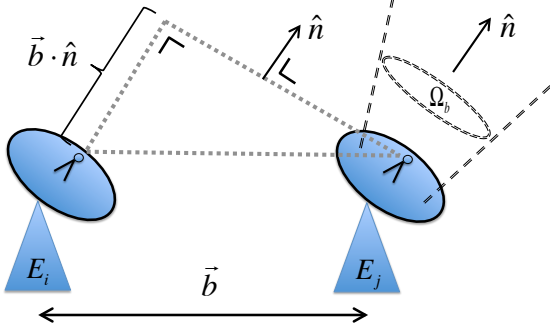


Figure 7. Schematic of a two-antenna interferometer.

be unity. Furthermore,  $\frac{2\pi\nu}{c}(b_x\theta_x + b_y\theta_y) \equiv 2\pi(u\theta_x + v\theta_y)$  is the phase delay between two antennae (position in the  $uv$  plane measures the phase lag between the two dishes in wavelengths). The coefficient of proportionality in the above equation is set by various instrumental parameters and is not relevant for our purposes. From Eq. (A2), it follows that

$$\rho_{ij}(\nu) = \frac{\int_{\Omega_{\text{beam}}} d\theta_x d\theta_y \mathcal{I}(\theta_x, \theta_y, \theta_\nu) e^{2\pi i(u\theta_x + v\theta_y)}}{\int_{\Omega_{\text{beam}}} d\theta_x d\theta_y \mathcal{I}(\theta_x, \theta_y, \theta_\nu)}, \quad (\text{A8})$$

where the denominator in the above formula approximately integrates to (for a small beam)

$$\int_{\Omega_{\text{beam}}} d\theta_x d\theta_y \mathcal{I}(\theta_x, \theta_y, \theta_\nu) \approx \Omega_{\text{beam}} \mathcal{I}(\theta_x, \theta_y, \theta_\nu). \quad (\text{A9})$$

We can now use the approximate expression for the resolution of a single dish,

$$\Omega_{\text{beam}} = \frac{\lambda^2}{A_e}, \quad (\text{A10})$$

the Rayleigh-Jeans law (or the definition of the brightness temperature),

$$\mathcal{I}(\theta_x, \theta_y, \theta_\nu) = \frac{2k_B T_{\text{sky}}}{\lambda^2}, \quad (\text{A11})$$

and note that the numerator in Eq. (A8) matches the definition of visibility from Eq. (6), to get

$$\rho_{ij}(\nu) = \frac{A_e}{2k_B T_{\text{sky}}} \mathcal{V}(u, v, \theta_\nu), \quad (\text{A12})$$

Combining the above expression and Eq. (A6), we get the final result of this derivation,

$$\begin{aligned} \langle |\mathcal{V}(u, v, \theta_\nu)|^2 \rangle &= \frac{1}{\Omega_{\text{beam}}} \left( \frac{2k_B T_{\text{sky}}}{A_e \sqrt{t_1 \Delta\nu}} \right)^2 \\ &\times \delta_D(u - u') \delta_D(v - v') \delta_{\theta_\nu \theta_{\nu'}}, \end{aligned} \quad (\text{A13})$$

where the visibility  $\mathcal{V}$  is a complex Gaussian variable, centered at zero, and uncorrelated for different values of its arguments, and the factor of  $\Omega_{\text{beam}}$  came from converting from Kronecker delta to a Dirac delta function.

It should be noted at the end that we were calculating the contribution to the visibility from the noise only (the system temperature + the foreground sky temperature, in the absence of a signal). In case we want to repeat the computation in the presence of a signal,  $T_{\text{sky}}$  should instead be the sum of the signal and the noise temperatures.

## Appendix B: Contamination from Lensing

We now consider gravitational lensing of the 21-cm signal by the large scale structure, as a source of noise in searches for magnetic fields using the method proposed in this work. We first compute the transverse shear power spectrum and then evaluate the bias it produces for the magnetic-field estimator. We demonstrate that this bias can be expected to be negligible, even for arrays with very futuristic collecting areas of  $\sim 100 \text{ km}^2$ .

To follow standard lensing notation, we no longer label cartesian coordinate axes with  $x$ ,  $y$ , and  $z$ , but rather with numbers, using the convention where directions 1 and 2 lie in the plane of the sky, while 3 lies along the line of sight. Specifically, we use angular coordinates  $(\theta_1, \theta_2)$  to denote direction in the sky  $\hat{\mathbf{n}}$ , and  $\theta_3$  to denote a comoving interval  $r_z/\chi(z)$  along the line of sight, located at redshift  $z$ , and corresponding to  $\Delta z$  interval. As before, we denote variables in Fourier space with tilde, and use  $\vec{\ell} \equiv (\ell_1, \ell_2)$  for a conjugate variable of  $\hat{\mathbf{n}}$ .

We start by generalizing the formalism for two-dimensional weak lensing [39] to the three-dimensional case. In the presence of lensing, coordinate  $\theta_i^S$ , where  $i \in \{1, 2, 3\}$ , maps onto the observed coordinate  $\theta_i$  as follows

$$\theta_k^S = \theta_k + \frac{\partial \psi}{\partial \theta_k}, \quad k = 1, 2, \quad \theta_3^S = \theta_3 \quad (\text{B1})$$

where  $\psi$  is the lensing potential. The full Jacobian of this coordinate transformation is

$$\begin{aligned} \frac{\partial \theta_i^S}{\partial \theta_j} &= \delta_{ij} + \begin{pmatrix} \psi_{,11} & \psi_{,12} & \psi_{,13} \\ \psi_{,21} & \psi_{,22} & \psi_{,23} \\ 0 & 0 & 0 \end{pmatrix}_{ij} \\ &= I_{ij} + \begin{pmatrix} \kappa & 0 & 0 \\ 0 & \kappa & 0 \\ 0 & 0 & 0 \end{pmatrix}_{ij} + \begin{pmatrix} \gamma_{11} & \gamma_{12} & \gamma_{13} \\ \gamma_{12} & \gamma_{22} & \gamma_{23} \\ 0 & 0 & 0 \end{pmatrix}_{ij}, \\ &(i, j = 1, 2, 3), \end{aligned} \quad (\text{B2})$$

where  $I_{ij}$  represents the unity matrix. In the second step in Eq. (B2), we decomposed the  $2 \times 2$  upper-left sub-matrix into a sum of a diagonal matrix and a traceless symmetric matrix  $\gamma_{2 \times 2}$ , representing magnification and 2-dimensional shear, respectively. Along with the two



transverse shear components, they form into a  $3 \times 3$  shear matrix  $\gamma$ .

We now switch to Fourier space, where the two-dimensional Fourier transform of the lensing potential reads

$$\tilde{\psi}(\vec{\ell}, z) \equiv \int \psi(\hat{\mathbf{n}}, z) e^{-i\vec{\ell} \cdot \hat{\mathbf{n}}} d\theta_1 d\theta_2. \quad (\text{B3})$$

The relation between  $\psi$  and the Newtonian potential  $\Phi$  in a flat universe is

$$\psi(\hat{\mathbf{n}}, z) = -2 \int_0^{\chi(z)} d\chi_1 \left[ \frac{1}{\chi_1} - \frac{1}{\chi} \right] \Phi(\hat{\mathbf{n}}, \chi_1), \quad (\text{B4})$$

where  $\chi_1$  is an integration variable. Combining Eqs. (B3) and (B4), we get

$$\frac{\partial \tilde{\psi}(\vec{\ell}, z)}{\partial \theta_3} = -\frac{2}{\chi(z)} \int_0^{\chi(z)} d\chi_1 \tilde{\Phi}(\vec{\ell}, \chi_1). \quad (\text{B5})$$

From Eqs. (B5) and (B2), it follows

$$\begin{aligned} \langle \tilde{\gamma}_{13}^*(\vec{\ell}, z) \tilde{\gamma}_{13}(\vec{\ell}', z') \rangle &= \left\langle \ell_1 \ell'_1 \frac{\tilde{\psi}^*(\vec{\ell}, z)}{\partial \theta_3} \frac{\tilde{\psi}(\vec{\ell}', z')}{\partial \theta_3} \right\rangle \\ &= \frac{4\ell_1 \ell'_1}{\chi(z)\chi(z')} \int_0^{\chi(z)} d\chi_1 \int_0^{\chi(z')} d\chi'_1 \langle \tilde{\Phi}^*(\vec{\ell}, \chi_1) \tilde{\Phi}(\vec{\ell}', \chi'_1) \rangle. \end{aligned} \quad (\text{B6})$$

We now define the three-dimensional Fourier transform of the Newtonian potential  $\tilde{\Phi}$  through

$$\tilde{\Phi}(\vec{\ell}, \chi) \equiv \int \tilde{\Phi}(\vec{\ell}, \ell_3) e^{i\ell_3 \chi} \frac{d\ell_3}{2\pi}, \quad (\text{B7})$$

where  $\ell_3$  is an integration variable. Using this definition, we get

$$\begin{aligned} \langle \tilde{\Phi}^*(\vec{\ell}, \chi) \tilde{\Phi}(\vec{\ell}', \chi') \rangle &= \int \int \frac{d\ell_3}{2\pi} \frac{d\ell'_3}{2\pi} \langle \tilde{\Phi}^*(\vec{\ell}, \ell_3) \tilde{\Phi}(\vec{\ell}', \ell'_3) \rangle \\ &\quad \times e^{i(\ell'_3 \chi' - \ell_3 \chi)}. \end{aligned} \quad (\text{B8})$$

Assuming different modes are uncorrelated, we get

$$\begin{aligned} \langle \tilde{\Phi}^*(\vec{\ell}, \ell_3) \tilde{\Phi}(\vec{\ell}', \ell'_3) \rangle \\ = (2\pi)^3 \delta(\ell_3 - \ell'_3) \delta^2(\vec{\ell} - \vec{\ell}') P_\Phi(\sqrt{\ell_3^2 + \ell'^2}). \end{aligned} \quad (\text{B9})$$

where

$$\begin{aligned} P_\Phi(\ell) &= \frac{P_\Phi(k = \ell/\chi(z))}{\chi(z)^2} \\ &= \left[ \frac{3}{2} \Omega_m H_0^2 (1+z) \right]^2 \frac{P_\delta(k, z)}{k^4 \chi(z)^2}, \end{aligned} \quad (\text{B10})$$

is the angular power spectrum. Substituting Eq. (B9) into (B8) and applying Limber approximation  $\ell_3 \ll \ell$ , we obtain

$$\langle \tilde{\Phi}^*(\vec{\ell}, \chi) \tilde{\Phi}(\vec{\ell}', \chi') \rangle = (2\pi)^2 \delta^2(\vec{\ell} - \vec{\ell}') P_\Phi(\ell) \delta(\chi' - \chi), \quad (\text{B11})$$

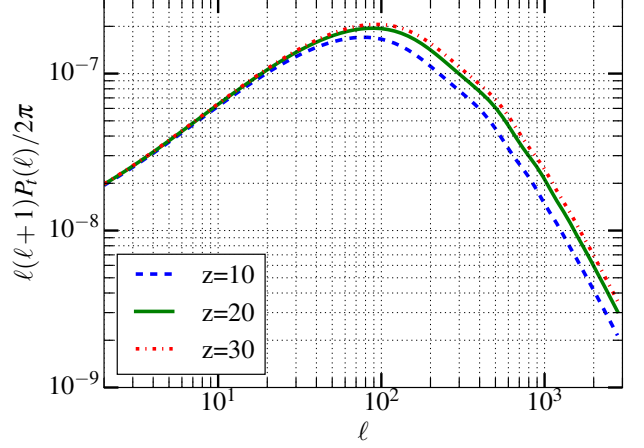


Figure 8. The transverse power spectra for sources at redshifts  $z = 10, 20$  and  $30$ , computed for standard cosmology.

Thus, for  $z \leq z'$ ,

$$\begin{aligned} \langle \tilde{\gamma}_{13}^*(\vec{\ell}, z) \tilde{\gamma}_{13}(\vec{\ell}', z') \rangle \\ = \frac{4}{\chi(z)\chi(z')} \ell_1 \ell'_1 (2\pi)^2 \delta^2(\vec{\ell} - \vec{\ell}') \int_0^{\chi(z)} d\chi_1 P_\Phi(\ell). \end{aligned} \quad (\text{B12})$$

We are interested in calculating the power spectrum  $P_{13}(\vec{\ell}, z, z')$  of  $\gamma_{13}$  components, defined as

$$\langle \tilde{\gamma}_{13}^*(\vec{\ell}, z) \tilde{\gamma}_{13}(\vec{\ell}', z') \rangle \equiv (2\pi)^2 P_{13}(\vec{\ell}, z, z') \delta^2(\vec{\ell} - \vec{\ell}'). \quad (\text{B13})$$

From Eq. (B12) we can express

$$P_{13}(\vec{\ell}, z, z') = \frac{4\ell_1^2}{\chi(z)\chi(z')} \int_0^{\chi(z)} d\chi_1 P_\Phi(\ell), \quad (\text{B14})$$

where, as before,  $\chi_1$  is an integration variable. Similar result holds for the power spectrum  $P_{23}$  of  $\gamma_{23}$  component. Finally, the transverse power spectrum  $P_t$  can be expressed as

$$\begin{aligned} P_t(\ell, z, z') &\equiv P_{13} + P_{23} \\ &= \frac{4\ell^2}{\chi(z)\chi(z')} \int_0^{\chi(z)} d\chi_1 P_\Phi(\ell). \end{aligned} \quad (\text{B15})$$

If  $z = z'$ , the above expression simplifies to

$$P_t(\ell, z) = \frac{4\ell^2}{\chi(z)^2} \int_0^{\chi(z)} d\chi_1 P_\Phi(\ell). \quad (\text{B16})$$

In Figure 8, we show the transverse power spectra for a range of  $z$ , for standard cosmology.

Now that we have computed the transverse power spectrum  $P_t$ , we move on to evaluating the contamination it produces for the measurement of the magnetic field. We consider a configuration where the magnetic field is

along the direction 2,  $\hat{\mathbf{k}} = (\sin \varphi, 0, \cos \varphi)$ , and the line of sight is along the direction 3,  $\hat{\mathbf{n}} = (0, 0, 1)$  in the three-dimensional Cartesian reference frame where  $x$ ,  $y$ , and  $z$  axes correspond to 3, 1, and 2, respectively;  $\varphi$  is the angle between 3 and  $\hat{\mathbf{k}}$ . Lensing distorts  $\hat{\mathbf{k}}$  and  $\hat{\mathbf{n}}$  into

$$\begin{aligned}\hat{\mathbf{k}}' &= \begin{pmatrix} (1 + \kappa + \gamma_{11}) \sin \varphi + \gamma_{13} \cos \varphi \\ \gamma_{12} \sin \varphi + \gamma_{23} \cos \varphi \\ \cos \varphi \end{pmatrix}, \\ \hat{\mathbf{n}}' &= \begin{pmatrix} \gamma_{13} \\ \gamma_{23} \\ 1 \end{pmatrix},\end{aligned}\quad (\text{B17})$$

and the shear only changes  $\varphi$  by  $-\gamma_{13}$ , to first order.

For conciseness, we define the coefficient  $\bar{x}_B \equiv x_B/B$ , and introduce the following short notation

$$\begin{aligned}C &\equiv 0.128 \text{ mK} \left( \frac{T_\gamma}{T_s} \right) x_{1s} \left( \frac{1+z}{10} \right)^{1/2}, \\ \mu_0 &\equiv 39.6 - 3C - \frac{C}{60} \frac{1}{1 + x_{\alpha,(2)} + x_{c,(2)}}, \\ \mu_1 &\equiv 13.2 - C - \frac{C}{20} \frac{1}{1 + x_{\alpha,(2)} + x_{c,(2)}}, \\ \mu_2 &\equiv \frac{C}{10} \frac{x_B}{(1 + x_{\alpha,(2)} + x_{c,(2)})^2}.\end{aligned}\quad (\text{B18})$$

For the configuration we chose, the transfer function in the presence of a small magnetic field reads

$$\begin{aligned}G^{(B)} &= \left( 1 - \frac{T_\gamma}{T_s} \right) x_{1s} \left( \frac{1+z}{10} \right)^{1/2} \\ &\times (\mu_0 + \mu_1 \cos 2\varphi + \mu_2 \sin 2\varphi),\end{aligned}\quad (\text{B19})$$

where the  $\sin 2\varphi$  term represents a precession of the emission quadrupole by a small angle  $\epsilon$ , in the sense that  $\mu_1 \cos 2\varphi + \mu_2 \sin 2\varphi = \sqrt{\mu_1^2 + \mu_2^2} \cos[2(\varphi + \epsilon)]$ , where  $2\epsilon \simeq \tan(2\epsilon) = -\mu_2/\mu_1$ . Similarly, lensing also gives rise to  $\sin 2\varphi$  term, such that

$$\begin{aligned}G^{(\text{lens}, 13)} &= \left( 1 - \frac{T_\gamma}{T_s} \right) x_{1s} \left( \frac{1+z}{10} \right)^{1/2} \\ &\times [\mu_0 + \mu_1 (\cos 2\varphi + 2\gamma_{13} \sin 2\varphi)].\end{aligned}\quad (\text{B20})$$

In addition, it affects the magnitude  $k$ , such that

$$k' = k[1 + 2(\kappa + \gamma_{11}) \sin^2 \varphi + 2\gamma_{13} \sin \varphi \cos \varphi]. \quad (\text{B21})$$

to first order. Assuming  $P_\delta(k) \propto k^{n_{\text{eff}}}$ , due solely to the lensing-shear 13 component (and no magnetic field), we get

$$\begin{aligned}P^S(\vec{k}') &= \left| G^{(\text{lens}, 13)} \times [1 + 2(\kappa + \gamma_{11}) \sin^2 \varphi \right. \\ &\left. + 2\gamma_{13} \sin \varphi \cos \varphi]^{n_{\text{eff}}/2} \right|^2 P_\delta(k) \equiv |G'^{(\text{lens})}(\hat{\mathbf{k}}')|^2 P_\delta(k).\end{aligned}\quad (\text{B22})$$

where  $n_{\text{eff}}$  is an effective spectral index (which is a function of the range of  $k$  and redshift of interest; in our

case,  $n_{\text{eff}} \sim -2.274$ ). Expanding  $G'^{(\text{lens})}$ , we find the  $\sin 2\varphi$  term produced by the transverse lensing shear component, which mimics the precession effect due to the magnetic field, such that  $\mu_2/\mu_1 = [2 + n_{\text{eff}}\mu_0/(2\mu_1)]\gamma_{13}$ , where we can solve for the spurious “comoving magnetic field”,

$$\begin{aligned}B^{(\text{lens}, 13)} &= \frac{10(1 + x_{\alpha,(2)} + x_{c,(2)})^2 (2\mu_1 + \frac{n_{\text{eff}}}{2}\mu_0)}{C\bar{x}_B(1+z)^2} \gamma_{13} \\ &\equiv \alpha \gamma_{13}.\end{aligned}$$

Finally, the lensing contamination to the magnetic-field reconstruction from  $\gamma_{13}$  component is

$$P^{(\text{lens}, 13)}(\ell) = \left| \frac{\partial B^{(\text{lens}, 13)}}{\partial \gamma_{13}} \right|^2 P_{\gamma_{13}}(\ell) = \alpha^2 P_{\gamma_{13}}(\ell), \quad (\text{B23})$$

while the total power spectrum gets an average value, i.e. the half maximum,

$$P_B^{\text{lens}}(\ell) = \frac{\alpha^2}{2} P_t(\ell), \quad (\text{B24})$$

and the root-mean-square (rms) of the total contamination is

$$\Delta^{(\text{lens})}(\ell) = \sqrt{\frac{\ell(\ell+1)}{2\pi} P^{(\text{lens})}(\ell)}. \quad (\text{B25})$$

We show numerical results for the rms contamination in Figure 9, calculated with and without the de-lensing procedure (using CMB lensing measurements), with little difference found between the two cases. Comparing this result to Figure 6, we can see that the contamination due to lensing shear remains below the projected sensitivities even for the case of futuristic array sizes.

### Appendix C: Estimating the escape fraction of ionizing photons

In this appendix, we describe our method for estimating the escape fraction of ionizing photons in semi-numerical simulations of the high-redshift 21-cm signal, such as the publicly available 21cmFAST code [35].

Typically, such codes sidestep the computationally expensive tasks of tracking individual radiation sources, and the radiative transfer of the ionizing photons that are needed to simulate HII regions in the early Universe. Instead, they use an approximate relation between the statistics of HII regions and those of collapsed structures, and estimate the latter efficiently from pure large scale structure simulations [40]. As such, the escape fraction of ionizing photons is not a direct input to these simulations, but rather has to be indirectly estimated from their outputs and input effective parameters.

A HII region, say B, satisfies ionizing photon number-balance, i.e.,

$$N_{\text{emitted},B} = \langle f_{\text{esc},B} \rangle f_* N_{\gamma/b} f_{\text{coll},B} N_{b,B}, \text{ and} \quad (\text{C1a})$$

$$N_{\text{absorbed},B} = f_H (1 + \langle n_{\text{rec},B} \rangle) N_{b,B}. \quad (\text{C1b})$$

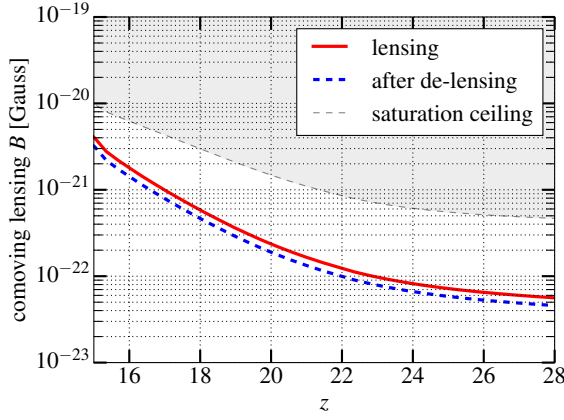


Figure 9. Shown is the  $1\sigma$  lensing-shear contamination to the measurement of the magnetic field, using the method discussed in this work. Contamination before (solid red line) and after (dashed blue line) the de-lensing procedure, is presented as a function of redshift. Saturation ceiling is denoted by the shaded region above the thin dashed line. Comparison with Figure 6 reveals that lensing is below the projected sensitivity for all array sizes considered in this work.

Here  $N_{\text{emitted,B}}$  and  $N_{\text{absorbed,B}}$  are total numbers of emitted and absorbed ionizing photons, i.e., those with energy  $> 13.6$  eV. In the above equations,  $f_{\text{H}} = 0.924$  is the hydrogen number-fraction,  $f_*$  is the star-formation efficiency (the fraction of galactic baryonic mass in stars),  $N_{\gamma/\text{b}}$  is the number of ionizing photons per nucleus produced by the stars,  $N_{\text{b,B}}$  is the total number of nuclei in B,  $\langle f_{\text{esc,B}} \rangle$  is the average escape fraction in B,  $\langle n_{\text{rec,B}} \rangle$  is the average number of recombinations per hydrogen atom inside, and  $f_{\text{coll,B}}$  is the collapse fraction. Also note that the photon numbers in Eqs. (C1) are integrated numbers over all redshifts up-to the redshift of interest.

We assume that once regions are ionized, they stay ionized. We also assume that the number of recombinations outside HII regions is negligible (we have numerically verified this in 21cmFAST runs, since the code tracks the ionization fraction outside HII regions).

Let  $\mathcal{B}(z)$  denote the set of all HII regions at redshift  $z$ . We obtain the total number of ionizing photons absorbed

upto a redshift  $z$  from Eq. (C1b):

$$N_{\text{absorbed,tot}}(z) = f_{\text{H}} \int_{\mathbf{r} \in \mathcal{B}(z)} dV n_{\text{b}} + f_{\text{H}}^2 \int_z^\infty dz' \left| \frac{dt}{dz'} \right| \int_{\mathbf{r} \in \mathcal{B}(z')} dV C n_{\text{b}}^2 \alpha_{\text{B}}, \quad (\text{C2})$$

where  $n_{\text{b}}$  is the baryon number density, the Jacobian  $|dt/dz|$  maps between redshift and proper time,  $C = \langle n^2 \rangle / \langle n \rangle^2$  is the clumping factor, and  $\alpha_{\text{B}}$  is the case-B recombination coefficient.

21cmFAST uses the ansatz that a self-ionized region satisfies  $f_{\text{coll}} = 1/\zeta$ , where  $\zeta$  is an efficiency factor. Using this in the volume-integrated version of Eq. (C1a), we obtain the total number of ionizing photons emitted in HII regions upto redshift  $z$  as

$$N_{\text{emitted,tot}}(z) = \frac{\overline{f_{\text{esc}}}(z) f_* N_{\gamma/\text{b}}}{\zeta} \int_{\mathbf{r} \in \mathcal{B}(z)} dV n_{\text{b}}, \quad (\text{C3})$$

where  $\overline{f_{\text{esc}}}(z)$  an ‘averaged escape fraction’ until each redshift. From Eq. (C2) and (C3), we get

$$\begin{aligned} \overline{f_{\text{esc}}}(z) &= \frac{f_{\text{H}} \zeta}{f_* N_{\gamma/\text{b}}} \left[ 1 + f_{\text{H}} \frac{\int_z^\infty dz' \left| \frac{dt}{dz'} \right| \int_{\mathbf{r} \in \mathcal{B}(z')} dV C n_{\text{b}}^2 \alpha_{\text{B}}}{\int_{\mathbf{r} \in \mathcal{B}(z)} dV n_{\text{b}}} \right] \\ &= \frac{f_{\text{H}} \zeta}{f_* N_{\gamma/\text{b}}} \left[ 1 + \frac{f_{\text{H}} n_{\text{b},0}}{\int_{\mathbf{x} \in \mathcal{B}(z)} d^3 \mathbf{x} [1 + \delta(\mathbf{x}, z)]} \times \right. \\ &\quad \left. \int_z^\infty dz' \left| \frac{dt}{dz'} \right| (1+z')^3 \int_{\mathbf{x} \in \mathcal{B}(z')} d^3 \mathbf{x} C [1 + \delta(\mathbf{x}, z')]^2 \alpha_{\text{B}} \right]. \end{aligned} \quad (\text{C4})$$

In the second line, we have rewritten the integrals in terms of co-moving coordinates and the over-density  $\delta(\mathbf{x}, z)$ .

An additional subtlety is that 21cmFAST follows the kinetic temperature outside the HII regions, while the recombination coefficient  $\alpha_{\text{B}}$  depends on the temperature inside; this can differ from the former due to the energy deposited by the free-electrons released during photoionization. We have verified that including this contribution makes little difference during the redshifts of interest.

- 
- [1] R. Durrer and A. Neronov, *Astron. and Astrophys. Review* **21**, 62 (2013), arXiv:1303.7121 [astro-ph.CO].
  - [2] J. P. Vallee, *New Astronomy Reviews* **48**, 763 (2004).
  - [3] A. Neronov and I. Vovk, *Science* **328**, 73 (2010), arXiv:1006.3504 [astro-ph.HE].
  - [4] R. Wielebinski, in *Cosmic Magnetic Fields*, Lecture Notes in Physics, Berlin Springer Verlag, Vol. 664, edited

- by R. Wielebinski and R. Beck (2005) p. 89.
- [5] R. Beck, *Space Science Reviews* **166**, 215 (2012).
- [6] K. Park, E. G. Blackman, and K. Subramanian, *Phys. Rev. E* **87**, 053110 (2013), arXiv:1305.2080 [physics.plasm-ph].
- [7] S. Naoz and R. Narayan, *Physical Review Letters* **111**, 051303 (2013), arXiv:1304.5792 [astro-ph.CO].



- [8] S. Naoz and R. Narayan, Physical Review Letters **111**, 051303 (2013), arXiv:1304.5792 [astro-ph.CO].
- [9] L. M. Widrow, D. Ryu, D. R. G. Schleicher, K. Subramanian, C. G. Tsagas, and R. A. Treumann, Space Science Reviews **166**, 37 (2012), arXiv:1109.4052 [astro-ph.CO].
- [10] T. Kobayashi, Journal of Cosmology and Astroparticle Physics **5**, 040 (2014), arXiv:1403.5168.
- [11] D. G. Yamazaki, K. Ichiki, T. Kajino, and G. J. Mathews, Advances in Astronomy **2010** (2010), arXiv:1112.4922 [astro-ph.CO].
- [12] P. Blasi, S. Burles, and A. V. Olinto, Astrophysical Journal, Letters **514**, L79 (1999), astro-ph/9812487.
- [13] F. Tavecchio, G. Ghisellini, L. Foschini, G. Bonnoli, G. Ghirlanda, and P. Coppi, MNRAS **406**, L70 (2010), arXiv:1004.1329 [astro-ph.CO].
- [14] K. Dolag, M. Kachelriess, S. Ostapchenko, and R. Tomàs, Astrophysical Journal, Letters **727**, L4 (2011), arXiv:1009.1782 [astro-ph.HE].
- [15] K. E. Kunze and E. Komatsu, Journal of Cosmology and Astroparticle Physics **1**, 009 (2014), arXiv:1309.7994 [astro-ph.CO].
- [16] T. Kahnashvili, Y. Maravin, A. Natarajan, N. Battaglia, and A. G. Tevzadze, Astrophys. J. **770**, 47 (2013), arXiv:1211.2769 [astro-ph.CO].
- [17] M. Shiraishi, H. Tashiro, and K. Ichiki, Phys. Rev. D **89**, 103522 (2014), arXiv:1403.2608.
- [18] H. Tashiro and N. Sugiyama, Mon. Not. R. Astron. Soc. **372**, 1060 (2006), astro-ph/0607169.
- [19] D. R. G. Schleicher, R. Banerjee, and R. S. Klessen, Astrophys. J. **692**, 236 (2009), arXiv:0808.1461.
- [20] Planck Collaboration, P. A. R. Ade, N. Aghanim, M. Arnaud, F. Arroja, M. Ashdown, J. Aumont, C. Baccigalupi, M. Ballardini, A. J. Banday, and et al., ArXiv e-prints (2015), arXiv:1502.01594.
- [21] T. Venumadhav, A. Oklopčić, V. Gluscevic, A. Mishra, and C. M. Hirata, ArXiv e-prints (2014), arXiv:1410.2250.
- [22] P. Madau, A. Meiksin, and M. J. Rees, Astrophys. J. **475**, 429 (1997), astro-ph/9608010.
- [23] A. Loeb and M. Zaldarriaga, Physical Review Letters **92**, 211301 (2004), astro-ph/0312134.
- [24] L. J. Greenhill and G. Bernardi, ArXiv e-prints (2012), arXiv:1201.1700 [astro-ph.CO].
- [25] J. D. Bowman, M. F. Morales, J. N. Hewitt, and MWA Collaboration, in *American Astronomical Society Meeting Abstracts #218* (2011) p. 132.06.
- [26] A. R. Parsons, A. Liu, J. E. Aguirre, Z. S. Ali, R. F. Bradley, C. L. Carilli, D. R. DeBoer, M. R. Dexter, N. E. Gugliucci, D. C. Jacobs, P. Klima, D. H. E. MacMahon, J. R. Manley, D. F. Moore, J. C. Pober, I. I. Stefan, and W. P. Walbrugh, Astrophys. J. **788**, 106 (2014), arXiv:1304.4991.
- [27] C. L. Carilli, ArXiv e-prints (2008), arXiv:0802.1727.
- [28] K. Vanderlinde and Chime Collaboration, in *Exascale Radio Astronomy* (2014) p. 10102.
- [29] D. R. DeBoer and HERA, in *American Astronomical Society Meeting Abstracts*, American Astronomical Society Meeting Abstracts, Vol. 225 (2015) p. 328.03.
- [30] H. Yan and A. Lazarian, Astrophys. J. **677**, 1401 (2008), arXiv:0711.0926.
- [31] H. Yan and A. Lazarian, J. Quant. Spec. Rad. Trans. **113**, 1409 (2012), arXiv:1203.5571 [astro-ph.GA].
- [32] M. Tegmark and M. Zaldarriaga, Phys. Rev. D **79**, 083530 (2009), arXiv:0805.4414.
- [33] T. Okamoto and W. Hu, Phys. Rev. D **67**, 083002 (2003), astro-ph/0301031.
- [34] Y. Mao, M. Tegmark, M. McQuinn, M. Zaldarriaga, and O. Zahn, Phys. Rev. D **78**, 023529 (2008), arXiv:0802.1710.
- [35] A. Mesinger, S. Furlanetto, and R. Cen, Mon. Not. R. Astron. Soc. **411**, 955 (2011), arXiv:1003.3878.
- [36] Planck Collaboration, P. A. R. Ade, N. Aghanim, M. Arnaud, M. Ashdown, J. Aumont, C. Baccigalupi, A. J. Banday, R. B. Barreiro, J. G. Bartlett, and et al., ArXiv e-prints (2015), arXiv:1502.01589.
- [37] F. Haardt and P. Madau, Astrophys. J. **746**, 125 (2012), arXiv:1105.2039.
- [38] K. M. Górski, E. Hivon, A. J. Banday, B. D. Wandelt, F. K. Hansen, M. Reinecke, and M. Bartelmann, Astrophys. J. **622**, 759 (2005), astro-ph/0409513.
- [39] D. H. Weinberg, M. J. Mortonson, D. J. Eisenstein, C. Hirata, A. G. Riess, and E. Rozo, Physics Reports **530**, 87 (2013), observational Probes of Cosmic Acceleration.
- [40] S. R. Furlanetto, M. Zaldarriaga, and L. Hernquist, Astrophys. J. **613**, 1 (2004), astro-ph/0403697.